U.PORTO

FEUP FACULDADE DE ENGENHARIA
UNIVERSIDADE DO PORTO

Turbulent Flow Acceleration Measurements with Single-Particle Doppler Anemometry DTU Wind Energy

July 18, 2014

Tiago João Ayres Pereira da Cunha Ramos

Dissertação do MIEM
Orientador na DTU: Prof. Jakob Mann
Orientador na FEUP: Prof. José Palma

Faculdade de Engenharia da Universidade do Porto
Mestrado Integrado em Engenharia Mecânica

[blank page]

Turbulent Flow Acceleration Measurements with Single-Particle Doppler Anemometry DTU Wind Energy

Tiago João Ayres Pereira da Cunha Ramos

Integrated Masters Degree in
Mechanical Engineering
Faculty of Engineering, Universidade do Porto

[**blank page**]

Abstract

The lidar technology allows, in specific conditions, the wind speed and acceleration measurement. Nevertheless, the acceleration measurements were found to be influenced and conditioned by the atmospheric and operation conditions that affect their uncertainties.

Laboratory tests allowed the radiation pressure effect measurement in the particles, used to determine the speed and acceleration values, and its consequence in the final results. They also allowed to validate the signal processing algorithm and to quantify the measurements uncertainties.

This document presents an introduction to some turbulence concepts and to some used statistical and physical tools. After, a description of the equipment setup, the used algorithm, the development and validation tests, the data manipulation as well as the final field experiment are done.

Keywords: Lagrangian, acceleration, measurements, lidar, Risø, DTU, FEUP, single-particle anemometry, MIEM.

[**blank page**]

Resumo

A tecnologia lidar permite, em condições específicas, a medição da velocidade e da aceleração do vento. As medições da aceleração são, no entanto, influenciadas pelas condições atmosféricas e de operação que condicionam a sua incerteza.

Testes laboratoriais permitiram medir o efeito da pressão de radiação nas partículas utilizadas para as medições e a sua consequência no valor da velocidade e aceleração determinados. Permitiram também validar o algoritmo de processamento do sinal e quantificar as incertezas presentes nas medições.

Este documento apresenta uma introdução às escalas da turbulência e a conceitos estatísticos a elas inerentes, assim como algumas ferramentas físicas e matemáticas utilizadas. Posteriormente, uma descrição da configuração do equipamento, do algoritmo utilizado, dos testes de desenvolvimento e validação, da manipulação dos dados e da atividade experimental final é efetuada.

Palavras-Chave: Medições, Lagrangianas, aceleração, lidar, Risø, DTU, FEUP, MIEM, anemometria, velocimetria.

[**blank page**]

Acknoledgements

From all the people that I would like to mention in this small paragraph, I would especially like to thank Professor José Palma, for his contact, help and opportunity, to Professor Jakob Mann, for his acceptance, knowledge, patience and mentoring, and Post Doc Anders Tegtmeier Pedersen, for all his assistance, help and partnership.
A special thanks to my parents and family for all their support during my stay in Denmark.

[**blank page**]

Contents

List of Figures

List of Tables

[**blank page**]

Nomenclature

ADC	Analog to Digital Converter
DC	Direct Current
DFT	Discrete Fourier Transform
DHT	Discrete Hilbert Transform
DTU	Danmarks Tekniske Universitet / Technical University of Denmark
DNS	Direct Numerical Simulation
EML	Enhanced Mode Lidar
FWHM	Full Width at Half Maximum
HC	90° Hybrid Coupler
PDF	Probability Density Function
RIN	Relative Intensity Noise
CNR	Carrier to Noise Ratio
TKE	Turbulent kinetic energy
α	Angle between the light beam and the photodetector / Angle between the lidar beam and the tangent to the spinning wheel
α_0	Beam spot size at the exit of the telescope
β	Complementary angle between the photodetector the the particles velocity
δ	Dirac delta function
ϵ	Energy dissipation rate
η	Kolmogorov length scale
κ	Wavenumber
λ	Ligth wavelengtho or Taylor microscale
ν	Fluid kinematic viscosity
$\mathbf{\Phi}_{ij}$	Velocity spectrum tensor
ϕ	Phase shift due to the Doppler effect
ρ	Fluid density (mass per unit volume)
R_λ	Taylor scale Reynolds number
$\sigma(*)$	Absolute uncertainty of the variable *
τ_η	Kolmogorov time scale
θ	Argument between I and Q signals / Incident angle between radiation and a surface
$\bar{a}$, $\langle a \rangle$	Mean acceleration

$\langle a^2 \rangle$	Turbulent acceleration variance
A	Generic phasor amplitude
a_0	Universal constant for turbulent acceleration variance
a_c	Centripetal acceleration
c	Speed of light
C_K	Kolmogorov constant
$\frac{\partial}{\partial t}$	Time partial derivative
$\frac{D}{Dt}$	Material time derivative
l_{DI}	Length scale between inertial and dissipative ranges
$\mathrm{erf}(x)$	Gauss error function
$E(\kappa)$	Energy spectrum function
$\mathscr{F}$	Fourier transform
F	Lorentzian function
f_D	Doppler shift frequency
f_L	Local oscillator signal frequency
f_S	Scattered signal frequency
R_f	Beam focus range
$\mathscr{G}$	Gaussian function
g	Gravitational acceleration
$\mathscr{H}$	Hilbert transform
$\mathcal{I}_n(z)$	Modified Bessel function of the first kind
I	In-phase signal
$I(r,z)$	Beam irradiance
I_0	Beam irradiance on the waist
$I_p d$	Electric current produced by the photodiode
$\mathcal{L}$	Flow dimension
L	Local oscillator signal magnitude
l	Length scale
l_0	Energy containing range length scale
l_{EI}	Length scale between energy containing and inertial ranges
m	Mass
$\mathcal{P}$	Production rate

p	Pressure
$P(z)$	Laser power at distance z from its focus
P_0	Laser power in its focus
P_{abs}	Radiation pressure due to absorption
P_{ref}	Radiation pressure due to reflection
$\mathbf{Q}$	Linear momentum
Q	Quadrature signal
$\mathbf{R}_{ij}$	Two-point correlation function
r	Transverse distance from the beam axis
R_t	Turbulent Reynolds number
Re	Reynolds number
$\mathbf{S}$	Poynting vector / Energy flux density
S	Scattered signal magnitude
t	Time instant
$\mathcal{U}$	Flow speed
u_i'	Turbulent speed. Speed fluctuations around its mean.
$u(l)$	Velocity scale with length scale l
u_i	Fluid velocity in the i direction
u_0	Wind mean speed
u_{rms}	Turbulent velocity quadratic mean
V	Particles absolute velocity
V_a	Particles speed in the beam direction
v_η	Kolmogorov velocity scale
v_t	Tangential speed
$w(z)$	Gaussian beam radius at z
w_0	Beam waist radius in its focus
z	Axial distance to the Gaussian beam focus
z_R	Rayleigh range

[**blank page**]

Chapter 1

1 Introduction

This document is organized in for main chapters.

In Chapter 1 an introduction to some turbulence concepts and to some used statistical and physical tools is made.

Chapter 2 introduces a description of the equipment setup, the data acquisition method, the signal processing algorithm and some physical and mathematical models developed to predict the radiation pressure effect, due to the lidar radiation momentum, and uncertainties in the acceleration measurements.

In Chapter 3, the laboratory and field experiments are described, as well as their results presented and discussed.

Chapter 4 presents the final conclusions of this dissertation as well as some recommendations for future developing work.

1.1 The Navier-Stokes equation

In fluid dynamics, in order to provide a complete mathematical description for incompressible flows, the mass and momentum conservation equations are needed, here for Newtonian fluids.

Due to its convenience, the Einstein tensor notation is used. This implies that repeated Roman indices are to be summed over its extension. For representing a vector in its whole the typographic convention with the boldface type, as in $\mathbf{R}$ in section §1.2 is used. In this case the conservation of mass and Navier-Stokes equations can be simplified into:

$$\frac{\partial u_i}{\partial x_i} = 0 \tag{1.1}$$

$$\frac{Du_i}{Dt} = \underbrace{\frac{\partial u_i}{\partial t} + u_j \frac{\partial u_i}{\partial x_j}}_{\text{Unsteady + Convective}} = \underbrace{-\frac{1}{\rho}\frac{\partial p}{\partial x_i}}_{\text{Pressure gradient}} + \underbrace{g_i}_{\text{Body forces}} + \underbrace{\nu \frac{\partial^2 u_i}{\partial x_j \partial x_j}}_{\text{Viscous stress}} \tag{1.2}$$

where u_1, u_2 and u_3 represent the flow velocity components in an orthogonal coordinate system.

In theory the problem is "well-posed" since for the four unknowns (u_1, u_2, u_3 and p) there are also four equations. Due to the complex nature of the Navier-Stokes equations (nonlinear, second-order, partial differential and non-local) they are not amenable to exact mathematical solutions except in a few instances [18].

The Navier-Stokes equations may depend sensitively on the initial conditions so that, after a short time, two realizations of the flow with infinitesimally different initial conditions may be completely uncorrelated with each other. Changes in the external forcing or variations in the boundary conditions can produce flows that vary from smooth laminar flow to more complicated turbulence motions with an identifiable length or time scale [5].

Historically, investigations of turbulence have progressed through alternating advances in experimental measurements, theoretical descriptions, and most recently, the introduction of numerical simulation of turbulence on high-speed computers [5].

The objective of this work was to exploit the ability of the lidar technology to measure a fluid acceleration in a turbulent atmospheric flow, and to use those

measurements to determine a turbulence universal constant. The instrument used was a continuous-wave coherent monostatic lidar system that operates in a near-infrared band around 1.55 µm with an in-phase and quadrature modulation.

1.2 Turbulent dimensional analysis and statistics

One of the tools used to study turbulent flows is dimensional analysis. In some circumstances it is possible to argue that some aspects of the structure of turbulence only depend on a few independent variables or parameters [7]. In this section a brief description of one of these analyzes is made to easily introduce the statistical description of the flow's acceleration that is one of the main focuses of the presented work.

1.2.1 The energy cascade

Richardson (1922) introduced the **energy cascade** idea that the kinetic energy enters the turbulence through a production mechanism at the largest scales of motion and is then transferred to smaller eddies by inviscid processes until the smallest scales, identified by Kolmogorov, where the energy is dissipated due to the fluid viscosity. The term "eddy" lacks a precise definition but is conceived to be a turbulent motion localized within a spatial defined region. The region occupied by a large eddy can also contain smaller eddies [25].

The turbulent scales of length, time and velocity are an estimate of an eddy size, lifetime and velocity order-of-magnitude [31]. Three different main scales (relative to the energy containing range, the inertial subrange and the dissipation range) can be distinguished and defined using dimensional analysis as a function of the energy dissipation rate ϵ and the fluid kinematic viscosity ν.

The dissipation rate is considered to be a universal constant for each turbulent flow (in steady-state) and in most shear flows is nearly always of the same order of magnitude of its turbulence production rate $\mathcal{P}$ [7].

1.2.2 Energy containing range

Let us characterize the eddies in the largest size range by their lengthscale l_0 which is comparable to the flow dimension $\mathcal{L}$. In atmospheric boundary layer, for example, l_0 scales with the boundary-layer depth or the height above the ground [31]. The flow Reynolds number is defined as

$$Re = \frac{\mathcal{U}\mathcal{L}}{\nu} \tag{1.3}$$

where $\mathcal{U}$ is the flow speed , $\mathcal{L}$ its characteristic length and ν its kinematic viscosity. The Reynolds number can be used to describe the ratio between the inertial and the viscous forces in a flow and to characterize its turbulence.

The turbulent Reynolds number can be defined using the turbulent scales as

$$R_t = \frac{u(l)\, l}{\nu} \tag{1.4}$$

In the energy containing range, the R_t number is large, at least in the atmosphere, and the direct effects of viscosity are negligibly small. At this scale the large eddies (l_0) are anisotropic, unstable and break up, transferring their energy to smaller eddies. As their size decrease, both their velocity and time scale also decrease until they reach the size of $l_{EI} \approx \frac{1}{6} l_0$ where the universal equilibrium range begins. The indexes/suffixes EI and DI (later to be used) indicates the demarcation

between the energy (E) and the inertial (I) ranges and between the dissipation (D) and inertial (I) subranges [25].

The time scale in the energy containing range is often called the turnover time, is defined as l_0/u_{rms} and can be an estimate of the typical lifetime of a large eddy before it enters the universal equilibrium range. Here, u_{rms} is the flow turbulent velocity root mean square (rms) or quadratic mean. u_{rms} can be determined by

$$u_{rms} = \left(\overline{u_i' u_i'}\right)^{1/2} \tag{1.5}$$

where u_i' are the speed fluctuations around its mean.

$$u_i' = u_i - \langle u_i \rangle \tag{1.6}$$

The energy dissipation rate ϵ can be determined by the inviscid, energy containing eddies [31] by[1]

$$\epsilon \sim \frac{u_{rms}^3}{l_0} \tag{1.7}$$

1.2.3 Universal equilibrium range

The size range $l < l_{EI}$ is referred to as the universal equilibrium range and is where the energy cascade occurs. The two dominant processes are the energy transfer $\mathcal{T}$ to successively smaller eddies and their viscous dissipation. Kolmogorov stated that at sufficiently high Reynolds number, the small-scale turbulent motions are statistically isotropic and have a universal form that is uniquely determined by ν and ϵ. This last statement is often referred as the Kolmogorov's first similarity hypothesis [25].

The inertial subrange In the mid regions of a typical daytime atmospheric boundary layer $\left(R_t \sim 10^8\right)$, eddy sizes range from roughly $\sim$ 1 km to $\sim$ 1 mm. Within the inertial subrange they contribute negligibly to the turbulent kinetic energy (TKE) fluxes and viscous dissipation and assume values between 30 m to 3 cm [31], except close to the ground where the length scales decreases towards the surface.

The Kolmogorov's second similarity hypothesis stated that in every turbulent flow at sufficiently high Reynolds number, the statistics of the motions in the inertial subrange have a universal form that is uniquely determined by ϵ, independent of ν [25]. This property will be exploited in section 1.2.4 and has a direct connection to what is called the Kolmogorov's $5/3$ law.

This range include the Taylor's microscale λ, that he misidentified as the spatial scale of the dissipative eddies [29].

$$\lambda = \left(15\frac{\nu u_{rms}^2}{\epsilon}\right)^{1/2} \tag{1.8}$$

Since it is a well-defined quantity, the Taylor microscale is often used to characterize the flow through the Taylor scale Reynolds number [25]:

$$R_\lambda = \frac{u_{rms}\lambda}{\nu} \tag{1.9}$$

[1] The use of $\sim$ implies a proportionality coefficient being between 0.2 and 5, according to Wyngaard [31]

This is related to the turbulent Reynolds number by

$$R_\lambda = \sqrt{\frac{R_t}{15}} \tag{1.10}$$

The dissipative range By Kolmogorov's 1941 hypotheses, often referred as the K41 theory, the velocity scale v, the length scale η and respective time scale τ_η are defined as

$$\eta \equiv \left(\frac{\nu^3}{\epsilon}\right)^{1/4} \tag{1.11}$$

$$v_\eta \equiv (\nu\epsilon)^{1/4} \tag{1.12}$$

$$\tau_\eta \equiv \left(\frac{\nu}{\epsilon}\right)^{1/2} \tag{1.13}$$

and characterize the eddies dissipative motion. The R_t in this range is ~ 1, which confirms the strong influence of viscosity in the flow. In the atmospheric boundary layer, depending on the conditions, $\eta \sim 1\,\text{mm}$, $v \sim 1\,\text{cm/s}$ and $\tau_\eta \sim 0.1\,\text{s}$ [31]. The kinetic energy dissipation occurs between the length scales of l_{DI} and η, being the last the smallest eddy size before this dissipate into heat [25].

The length scale $\mathcal{L}$ and the Taylor microscale λ are then related to the kolmogorov's by

$$\frac{\mathcal{L}}{\eta} \equiv R_t^{3/4} \tag{1.14}$$

$$\frac{\lambda}{\eta} \equiv R_t^{1/4} \tag{1.15}$$

In this paper a specially attention is given to the length scales that are related to different behavior and shape of the kinetic energy spectrum in section 1.2.4 of the turbulent flow. The figure 1 represents the length scales previously defined and the TKE course in the ranges by them confined.

1.2.4 The kinetic energy spectrum

One statistic tool used in turbulence analysis that contains some information on the spatial structure of the random field is the two-point, one-time auto-covariance R_{ij}, often referred to as the two-point correlation:

$$\mathbf{R}_{ij}\left(\mathbf{r}, \mathbf{x}, t\right) \equiv \left\langle u_i\left(\mathbf{x}, t\right) u_j\left(\mathbf{x}+\mathbf{r}, t\right)\right\rangle \tag{1.16}$$

where u_i is the wind velocity in the direction i and angular brackets $\langle \cdots \rangle$ denote ensemble (over several measurements) averaging.

For homogeneous (i.e., statistically invariant under translations of the reference frame) and stationary turbulence, the two-point correlation is considered to be independent of $\mathbf{x}$ and t. It can be used to calculate the velocity spectrum $\mathbf{\Phi}_{ij}(\kappa)$, where κ represents the wavenumber $\kappa = {}^{2\pi}/_{l}$ that can be seen as the spatial frequency of a wave. The velocity spectrum tensor is the Fourier transform of the two-point correlation and is defined as

$$\mathbf{\Phi}_{ij}\left(\boldsymbol{\kappa}\right) = \frac{1}{\left(2\pi\right)^3} \iiint_{-\infty}^{\infty} \mathrm{e}^{-\mathrm{i}\boldsymbol{\kappa}\mathbf{r}} \mathbf{R}_{ij}\left(\mathbf{r}\right) \mathrm{d}\mathbf{r} \tag{1.17}$$

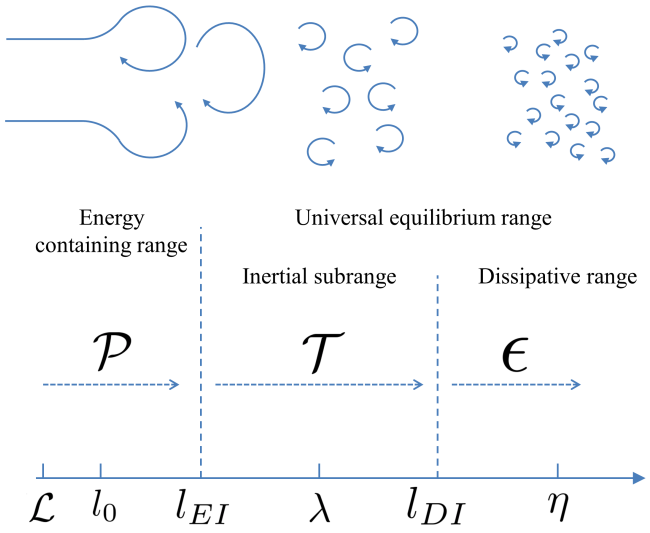

Figure 1: Different eddy sizes, ranges, length scales and TKE state.

and represents the contribution of the covariance $\langle u_i u_j \rangle$ of velocity modes with wave number κ [25].

One useful application of this tensor, in this paper, is its contribution to the definition of the energy spectrum function, defined as

$$E(\kappa) = \iiint_{-\infty}^{\infty} \frac{1}{2} \mathbf{\Phi}_{ij}(\boldsymbol{\kappa}) \, \delta(|\boldsymbol{\kappa}| - \kappa) \, \mathrm{d}\boldsymbol{\kappa} \tag{1.18}$$

that represents the contribution to the TKE per unit of mass, defined as $\frac{1}{2}\langle u_i u_i \rangle$, of eddies with wave number κ. δ represents the Dirac delta function, or the unit impulse function [25]. The energy spectrum can also be referred as the Kolmogorov's spectrum or the three-dimensional velocity spectrum [31]. Equation (1.18) shows that the energy spectrum function is obtained from $\mathbf{\Phi}_{ij}(\kappa)$ by removing all directional information. This is done by integration over all wavenumbers κ of magnitude $|\boldsymbol{\kappa}| = \kappa$ [25].

The turbulent kinetic energy can be calculated by integrating $E(\kappa)$ through all wavenumbers **[31]**.

$$\frac{1}{2}\langle u_i u_i \rangle = \frac{1}{2}\mathbf{R}_{ii}(r=0) = \int_0^{\infty} E(\kappa)\mathrm{d}\kappa \tag{1.19}$$

According to the Kolmogorov hypotheses, in any turbulent flow at sufficient high Reynolds number, the velocity spectra adopts particular universal forms. Figure 2 pretends to represent the expected shape of the energy spectrum.

Of special interest in this thesis is the inertial subrange properties in the velocity spectrum. A dimensional analysis, based on the Vaschy-Buckingham Π- theorem define $E(\kappa)$ as

$$E(\kappa) = C_K \epsilon^{2/3} \kappa^{-5/3} \tag{1.20}$$

where C_K is a universal constant called the Kolmogorov constant [14]. Experimental data support the value $C_K \equiv 1.5$ [25].

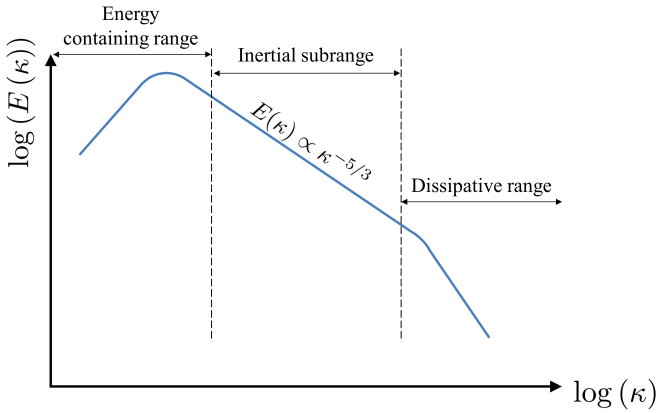

Figure 2: Energy spectrum sketch representation in a log-log scale.

The one-dimensional spectrum If only one component of the turbulent velocity is considered, the energy spectrum is then called "one-dimensional spectrum". Despite it has the same properties and power-law shape, its definition in (1.20) it has a different spectral constant [31].

Considering the wavenumber κ_1 as κ in the direction of the stream, the one-dimensional wavenumber spectra $E_{11}(\kappa_1)$ (longitudinal) and $E_{22}(\kappa_1)$ (transverse) are defined as

$$E_{11}(\kappa_1) = \frac{9}{55} C_K \epsilon^{2/3} \kappa_1^{-5/3} \tag{1.21}$$

$$E_{22}(\kappa_1) = \frac{12}{55} C_K \epsilon^{2/3} \kappa_1^{-5/3} \tag{1.22}$$

Please note that in some literature different normalizations of the one-dimensional spectra are used. The often cited, in this document, Pope ([25]) uses a form wherein the integral over the half-line is the variance $\langle u_i u_i \rangle$ (instead of the kinetic energy per unit of mass $\langle u_i u_i \rangle / 2$), in which case both (1.21) and (1.22) must be corrected by a factor of 2.

By the definition in (1.18), in this document, after experimental measurements the one dimensional energy spectrum was determined by

$$E_{ii}(\kappa_i) = \mathscr{F}\left[\mathbf{R}_{ii}(r=0)\right] = \frac{1}{2}\left|\hat{u_i}(k)\right|^2 \tag{1.23}$$

where $\hat{u_i}(k)$ represents the Fourier transform of the velocity in the direction i [9].

1.2.5 Acceleration statistics in turbulence

While turbulent velocity statistics may be approximated with Gaussian statistics [8], acceleration measurements can not. Acceleration probability density functions (PDF) are characterized by their long stretched exponential tails and usually represented in a log-linear plot normalized by the acceleration root mean square $\left\langle a^2 \right\rangle^{1/2}$. The figure 3 presents that typical shape for different Taylor microscale Reynolds numbers [30].

A suggested PDF function for turbulent acceleration parameters can be given by

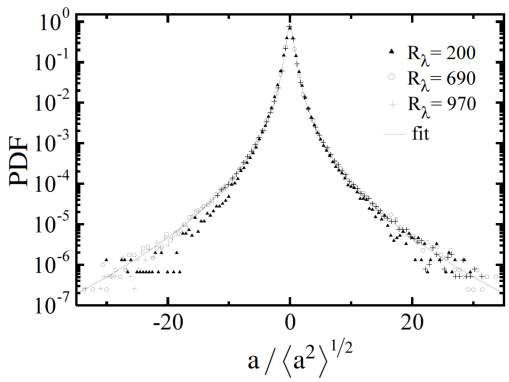

Figure 3: Probability density function of acceleration measurements at different R_λ [30].

$$P(a) = C \exp\left(\frac{-a^2}{(1 + |a\beta/\sigma|^\gamma \sigma^2)}\right) \tag{1.24}$$

where C, β, σ and γ are free parameters that can be determined by using a non-linear least squares routine, if intended to be used as a fitting function to real measurements [30]. As any PDF it can be used to determine the probability moments, specially the second moment or the variance by

$$\mathrm{Var}(a) = \int_{-\infty}^{+\infty} P(a) a^2 \mathrm{d}a \tag{1.25}$$

Another property of the function in (1.24) is that when multiplied by a^2 or a^4 it should drop to zero when a tends to $-\infty$ to $+\infty$. This can be easily seen in figure 4 below.

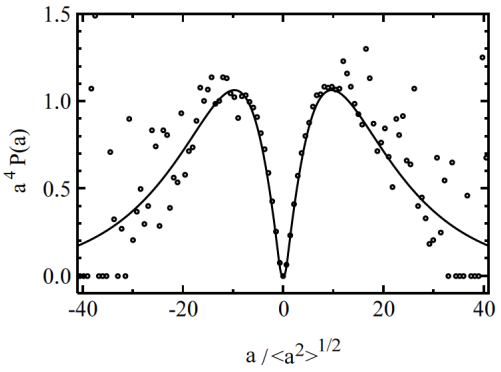

Figure 4: Acceleration PDF multiplied by a^4 to show which events are contributing to the acceleration flatness [30].

Let a_i denote a flow instantaneous acceleration measurement. Its biased variance can be given by

$$\mathrm{Var}(a) = \frac{1}{N} \sum_{i=1}^{N} (a_i - \langle a_i \rangle)^2 \tag{1.26}$$

where $\langle a_i \rangle$ is the acceleration mean. Using some statistics properties and the square brackets to denote ensemble average, (1.26) can be rewritten as

$$\mathrm{Var}(a) = \left\langle a^2 \right\rangle - \langle a \rangle^2 \tag{1.27}$$

Please note that onwards the subscript i will be dropped for simplification. In turbulent flows, the mean acceleration $\langle a \rangle$ is supposed to be zero in the absence of external forces that may interact with the flow. In the flows under investigation here the mean acceleration is negligible and therefore the acceleration variance will be simplified into $\left\langle a^2 \right\rangle$.

Kolmogorov scaling implies that the acceleration variance can also be expressed as a function of the energy dissipation rate ϵ and the fluid kinematic viscosity ν as in

$$\left\langle a^2 \right\rangle = a_0 \epsilon^{3/2} \nu^{-1/2} \tag{1.28}$$

where a_0 is an universal constant. This is also often referred as a universal Kolmogorov's constant but should not be confused with C_K in (1.20). Yaglom and Obukhov (1951) argued a_0 to be ≈ 1 for low Reynolds numbers if only one component of the acceleration is considered [19]. La Porta (2001) on the other hand stated that DNS (Direct Numerical Simulation) has found that a_0 depends on R_λ [12].

The figure 5 shows La Porta a_0 measurements in the axial component (squares) and transverse component (open circles), while DNS values are represented by the triangles and closed circles.

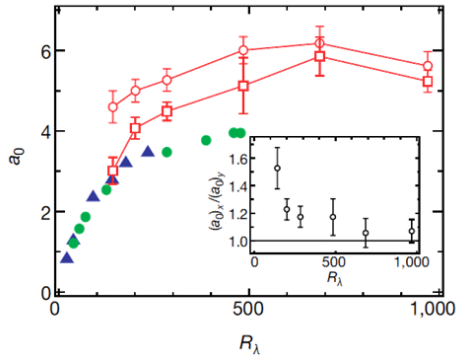

Figure 5: Constant a_0 as a function of R_λ [12].

1.3 Lidar systems for remote sensing

A lidar is a remote sensing technology normally used for measuring distances or velocity by analyzing the reflected light signal from a target when hit by a laser [28]. The present thesis objective lies specifically with systems for the measurement of atmospheric wind speed and acceleration. In the wind industry, it presents itself as an alternative or complement to the traditional methods for wind measurements that involve the siting of tall meteorological masts. It also allows the measurements at different directions and distances with a lidar in a single position. It is known by its capability for [22]:

- Resource assessment
- Wind turbine power curve measurement
- Advance wind speed detection for wind turbines

The instrument used for the measurements and tests performed in Risø DTU and presented in this document was a continuous-wave coherent monostatic lidar system that operates in a near-infrared band around 1.55 µm. The operating description and mentioned characteristics in this document will be directly related to this specific system.

Coherent lidar measures the Doppler shift frequency (section 1.3.1) by comparing the backscattered radiation frequency with the one from the reference beam [1]. A beam (section 1.3.2) of coherent radiation light the target and part of the reflected light is backscattered into a receiver. The target motion along the lidar beam direction leads to a change in the light's frequency via the Doppler shift. These alterations can be either a frequency increase, known as "blue shift", if the target moves towards the lidar, or a frequency decrease, known as "red shift", if the target moves away from the lidar. Both phenomena are due to the compression or extension, respectively, of the light wave [22].

When several targets or particles intersect the probe, the overall return signal exhibits a spectrum of frequencies resultant of the different contributions from different velocities. These have different intensity signals that can be determined by the weighting function in section 1.3.3.

1.3.1 The Doppler effect

The Doppler effect in optics is associated with the light propagation and accounts for the frequency shift when the light source is moving or light is reflected off a moving surface [33]. Figure 6 shows the geometrical interaction between the incident light and a particle and its resulting scattered light.

The Doppler shift f_D, depends on the speed V, and direction of the particle motion β, the light wavelength λ and the orientation of the observer α as represented in figure 6. For this configuration we have:

$$f_D = \frac{2V}{\lambda} \cos\beta \sin\left(\frac{\alpha}{2}\right) \tag{1.29}$$

This is calculated by the difference between the emitted and the measured (scattered) light frequencies [4].

For a lidar system operating in backscatter the angle α is equal to 180° and since only the axial component of the velocity is measured, the equation (1.29) can be simplified into:

$$f_D = \frac{2V_a}{\lambda} \tag{1.30}$$

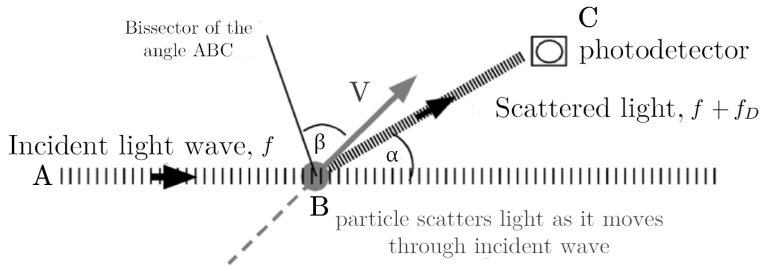

Figure 6: General representation of the Laser Doppler Anemometry (LDA) principle [3]

where V_a is the particle speed in the beam direction.

1.3.2 Gaussian Beam properties

When light wavefront normal make small angles with its optical axis its waves are called paraxial waves. A solution that satisfy the Helmholtz paraxial approximation for beam light behavior is denominated by Gaussian beam. The Helmholtz equation returns us the beam's electric field complex amplitude from which the irradiance of the beam in (1.34) can be derived.

Considering a z axis from the beam's focus point it is geometrical and physical properties are then presented.

The radius or spot size of the beam where the intensity drops to $1/e^2$ ($\approx 13.5\,\%$) of its value on the beam axis is given by [27]:

$$w(z) = w_0\sqrt{1 + \left(\frac{z}{z_R}\right)^2} \tag{1.31}$$

where w_0 is the minimum waist radius defined by the focus distance R_f, the beam wavelength λ and α_0 the spot size at the exit of the telescope. z_R is called the Rayleigh range.

$$w_0(R_f, \alpha_0) = \frac{\lambda R_f}{\pi \alpha_0} \tag{1.32}$$

$$z_R = \frac{\pi w_0^2}{\lambda} \tag{1.33}$$

These geometric parameters are represented in figure 7.

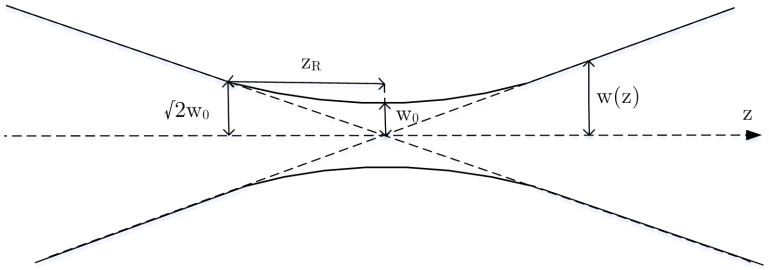

Figure 7: Gaussian beam radius as a function of the axial distance z.

The time-averaged intensity or irradiance of the beam I in (Wm^{-2}) can be written according to its value I_0 on the waist [26]

$$I(r,z) = I_0 \left(\frac{w_0}{w(z)}\right)^2 \exp\left(\frac{-2r^2}{w^2(z)}\right) \tag{1.34}$$

that resembles a Gaussian function.

A Gaussian function can be described according to the expression (1.35) and its similar to its probability distribution function (PDF) [21] except for its normalization (in which its integral is equal to 1).

$$\mathscr{G}(x,\mu,\sigma,a,b) = a\exp\left(-\frac{(x-\mu)^2}{2\sigma^2}\right) + b \tag{1.35}$$

where μ is the mean value, σ the standard deviation, a a geometric parameter and b the offset in order to the abscissa as shown in figure 8. The Gaussian PDF is a particular case of this where $b = 0$ and $a = 1/\sigma\sqrt{2\pi}$.

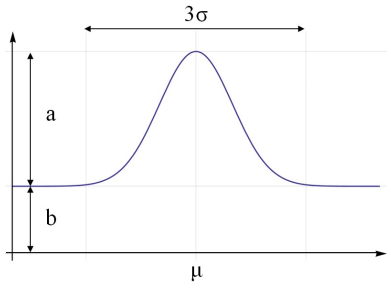

Figure 8: Gaussian function and its parameters.

The irradiance becomes more spread with increasing focus distance and decreases in the radial distance to the beam axis as we can see in figure 9.

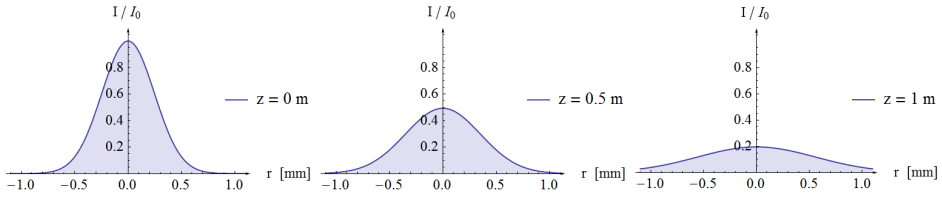

Figure 9: Normalized beam intensity along radial distance for three different axial distances.

Since $w(z)$ is defined as the beam radius where the intensity drops to $1/\mathrm{e}^2$ the laser power inside its confines is also function of z is also a part of the total power. For a circle of radius $r = w(z)$, the fraction of power, $P(z)$, transmitted through the circle can be defined as

$$P(z) = P_0\left(1 - \mathrm{e}^{-2}\right) = P_0\left(\frac{\mathrm{e}^2 - 1}{\mathrm{e}^2}\right) \tag{1.36}$$

The beam power $P(z)$ can be obtained integrating the irradiance (1.34) along waist of the beam. Taking that and the equation (1.36) , considering a flat surface normal to the beam, for $z = 0$:

$$P_0 = \frac{e^2}{1-e^2} \int_0^{w_0} I_0 \exp\left(\frac{-2r^2}{w_0^2}\right) 2\pi r \, \mathrm{d}r = \frac{I_0}{2}\pi w_0^2 \tag{1.37}$$

1.3.3 The Lorentzian axial weighting function

In the lidar system already referred the contribution from any target is weighted by the square beam's intensity at that point [8]. (This property is expressed in (2.4) in section 2.1.1). Since the laser beam is relatively narrow, the spatial dependence of sensitivity transverse to the beam can be ignored once compared with the axial one. A good approximation for the axial weighting function can be given by a Lorentzian function [11]:

$$F = \frac{z_R/\pi}{z^2 + z_R^2} \tag{1.38}$$

where z is the distance from the beam waist along the beam direction and $1/(\pi z_R)$ the maximum value of the function for $z = 0\,\mathrm{m}$. F is normalized so that its integral along all the beam length (from $-\infty$ to $+\infty$) it is equal to one. The Rayleigh range is a function of the system properties and the distance from the lidar output lens to the beam focus as described in section 1.3.2. Figure 10 shows a representation of the axial weighting function for a lidar beam focused at 4 m. The highlighted point shows that the value of the function at the Rayleigh range is half of its maximum.

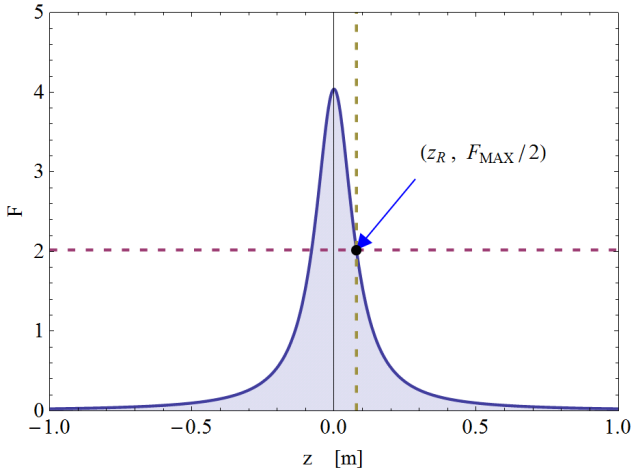

Figure 10: Lorentzian axial weighting function for a lidar beam focused at 4 m.

1.4 Single-particle anemometry

For short laser focus ranges (<8 m) the signal envelope provided by lidar measurements resembles a Gaussian function . This happens because the beam is Gaussian and therefore any particle that intersects it in a trajectory close to the transverse direction, with constant speed, would produce a Gaussian burst signal, similar to the one represented on the right of figure 11. Although the measured speed is in the beam direction, due to its slender shape it can be considered that particles seldom intersect the beam in a perfect longitudinal direction what would produce a Lorentzian burst shape instead.

For small ranges (<8 m), as the range is reduced, the measurement volume becomes small enough to be able to provide the signal due to a single particle interaction with the laser. This signal comes as a beat or a burst and can provide a high carrier-to-noise ratio (CNR) since the signal becomes concentrated within a small time window and its (frequency) bandwidth is reduced, compared with multi-particle detection [8].

The figure 11 shows the difference between two signals. The first represents the usual frequency signal from multi-particle scattering and the second the characteristic burst signal from single-particle scattering.

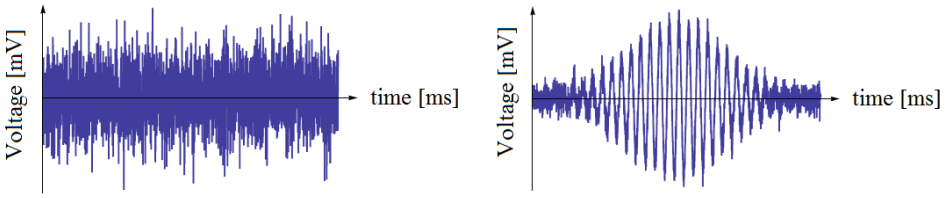

Figure 11: Time-domain signals of single-particle Doppler anemometry representations. Multi-particle scattered signal on the left and single-particle scattered signal on the right.

If a particle responsible for the signal experiences a change in its longitudinal speed, the scattered Doppler frequency will also shift. By measuring that variation it is possible to infer about its acceleration and therefore the wind acceleration in the small volume involved.

Figure 12 illustrates an ideal single-particle signal representation, obtained by simulation, with constant longitudinal speed and the Doppler frequency shift due to a speed increase.

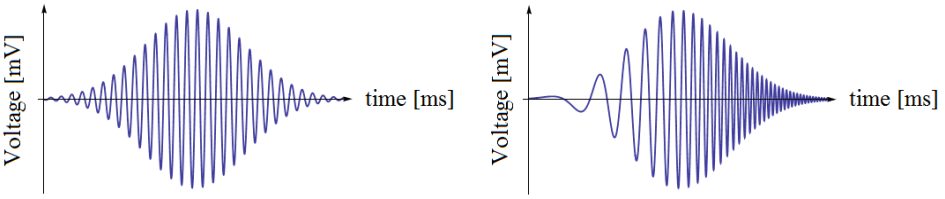

Figure 12: Constant signal frequency due to constant velocity on the left. Increase in signal frequency denotes particle acceleration on the right.

Chapter 2

2 Methodology

2.1 Acquiring the data

In this section a description of the equipment setup and the data acquisition procedure is made. They represent the technique used to measure and record the data that after processed returns the wind speed and acceleration values.

2.1.1 Equipment setup

Figure 13 shows a diagram with the different components that constitute the whole system. A brief explanation of their role is presented after.

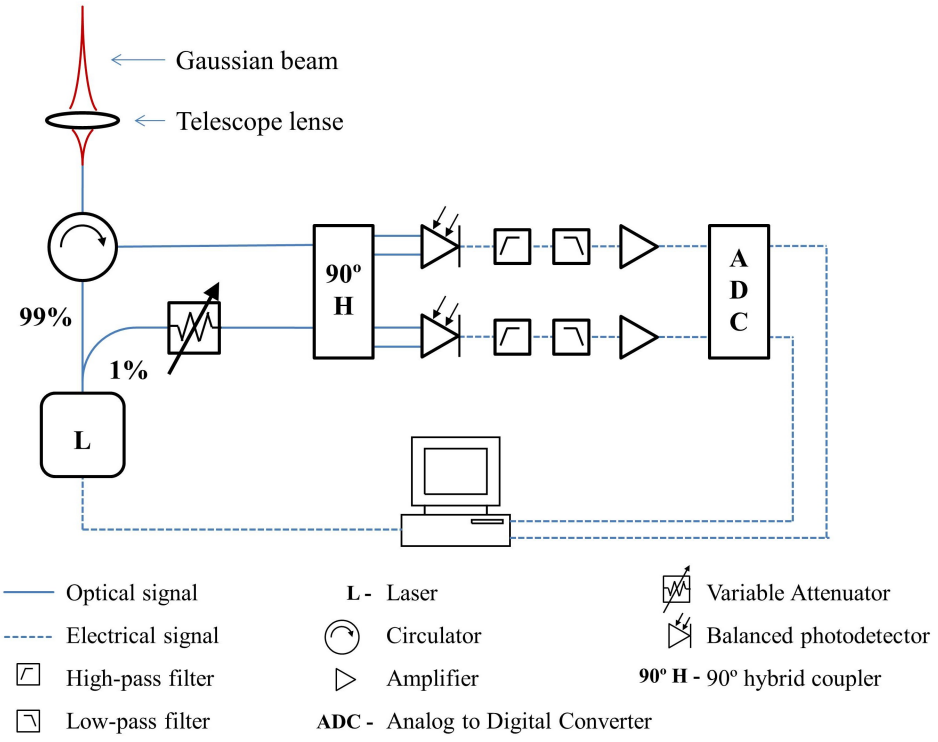

Figure 13: Equipment setup and its components

A *PXI* computer commands the laser imposing it a specific wavelength. The laser travels through the different components via an optical fiber represented as a solid line in figure 13.

After being generated the laser signal is divided in two components. The first, equivalent to 1 % of its intensity, goes to the variable attenuator and then to the 90° hybrid coupler (90°HC), to be used as an optical amplifier or coherent reference, and it is called the local oscillator. The remaining 99 % moves to the circulator.

In the circulator, light is only allowed to travel in one direction and therefore the light from the laser goes to the telescope lens where the Gaussian beam (section 1.3.2) is formed and its focusing range can be manually adjusted. On the other hand, the backscattered signal goes to the 90°HC where it is mixed with the

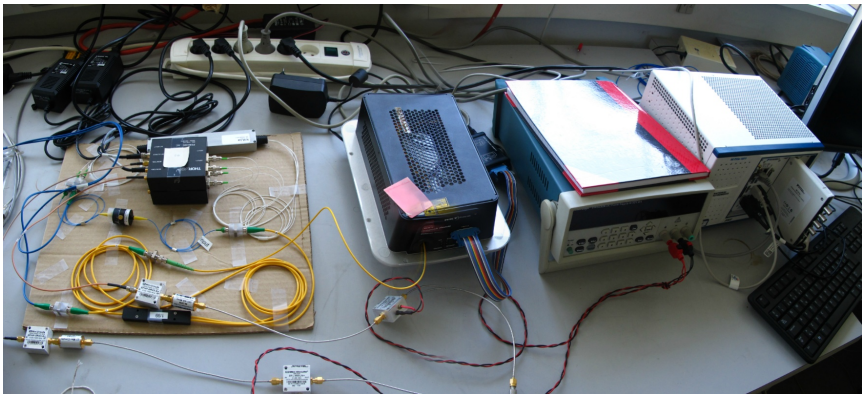

Figure 14: Lidar equipment setup used for the tests and measurements in Risø.

local oscillator that comes from the variable attenuator. This last is used to reduce and control the diverted laser to avoid a future signal saturation. The signals mix is required to manipulate and detect the backscattered signal since this has a low amplitude to be detected by itself in the following photodiodes. The detection method that uses this combined wave is called heterodyne or coherent detection.

Let expression (2.1) and (2.2) describe the electromagnetic waves of the local oscillator and the scattered signal respectively:

$$L(L, f_L, t) = L\mathrm{e}^{-\mathrm{j}(2\pi f_L t)} \tag{2.1}$$

$$S(S, f_S, t) = S\mathrm{e}^{-\mathrm{j}(2\pi f_S t+\phi)} \tag{2.2}$$

where j is the complex unit, L and S the signal magnitudes, f_L and f_S their frequency and ϕ an additional phase shift also due to light trajectory.

After being mixed together and polarized in the 90°HC, the light signal is converted into electric current using a photodiode. This electric current produced by the photodiode, I_{pd}, is proportional to the light power and thus to the absolute square of the mixed signal:

$$I_{pd} \propto \left| L\mathrm{e}^{-\mathrm{j}(2\pi f_L t)} + S\mathrm{e}^{-\mathrm{j}(2\pi f_S t+\phi)} \right|^2 \tag{2.3}$$

Using Euler's formula and some trigonometric properties it can be rewritten as

$$I_{pd} \propto \underbrace{L^2 \cos\left(-\mathrm{j}(4\pi f_L t)\right) + S^2 \cos\left(-\mathrm{j}(4\pi f_B t + 2\phi)\right)}_{\backsimeq \text{DC signal}} + \underbrace{+ 2LS \cos\left(-\mathrm{j}(2\pi\left(f_L - f_B\right) t - \phi)\right)}_{\text{signal with Doppler shift frequency}} \tag{2.4}$$

where $f_L - f_B = f_D$, the Doppler frequency shift. The ratio between f_L and f_D can be given by $f_L/f_D = c/2V_a$ where c is the speed of light in vacuum and V_a the velocity in (1.30). For wind speeds around 10 m/s this ratio is in the order of $\backsim 6 \times 10^6$ and therefore the first two components in (2.4) can be considered as a DC (direct current) offset, when averaged over short periods of time in the detector or low-pass filter.

The 90°HC act as a passive optical component with the purpose to produce two similar signals shifted by 90° or $\pi/2$ rad to be used as the in-phase (I) and

quadrature (Q) signal in section §2.2. This is done by using a device that alters the light wave polarization called waveplate.

The output signal is formed by two pairs of duplicated signals (two for the I and two for the Q signal) that go to the balanced photodetectors. The duplicated signals are also shifted by 180° or π rad to each other and are used in order to cancel some common noise in the laser and the DC offset before mentioned.

In order to simplify the following explanation only the I signal will be referred onward, since all the next operations are common to both I and Q.

Each balanced photodetector is composed by two photodiodes and one amplifier that convert the optical signal into an electric signal. The 180° shifted I signals produce two symmetric electric currents after the light have been absorbed in the photodiodes. With the proper polarization, when the two signals are subtracted, any common offset or noise in the laser is eliminated and the resultant signal is then amplified.

At the exit of the photodetector there are generally three noise contributions:

- Dark noise - or dark current noise is present even in the absence of incident light in the photodiodes. It results from random electron-hole pairs generated, for example, by thermal effects [26].

- Shot noise - The randomness of the incident photon stream in the photodiode is transformed into a fluctuating electric current. If the incident photons are Poisson distributed, these fluctuations are known as shot noise [26]. This leads to a spectrally flat output noisy signal [22] and it is proportional to the detected optical power [24].

- Laser relative intensity noise (RIN) - The transmitting laser contributes to noise in the system proportionally to its transmitted power peak. It is evaluated as a fraction of the laser power and is therefore termed as *relative intensity noise*. It is a consequence of inherent fluctuations in the output laser intensity and frequency [20].

The analog electric signal then pass through a band-pass filter created by combining a high-pass with a low-pass filter. If the two photodiodes produce a current signal with slightly different amplitudes the resulting signal will still have the DC offset that can be filtered in the high-pass filter, while the low-pass is used to attenuate any frequency above the Nyquist frequency (half of the sampling rate) to avoid an aliasing effect known as “folding” (observed in the frequency spectrum).

The electric signal is then amplified using a 12 V power supply and converted to a digital signal using a dual channel analog-digital converter (ADC) to be recorded by the computer.

The I signal is inputted trough the first channel and the Q through the second [23].

2.1.2 Data acquisition

When the digital signal returns the computer to be recorded it is composed by a list of 16-bit integers that, depending on the sampling rate and sample size, generates a large data creation rate [2] that would require a significant storage memory. In order to avoid this, the data is only recorded in small time periods (in $\sim$ ms time range) that contain a burst signal with useful information concerning the wind speed and acceleration.

[2] If a 120 MHz sampling rate is used each channel would produce $\sim$ 240 MBps if the burst were recorded continually.

The lidar system identifies the presence of a burst when the input digital signal in the computer exceeds a threshold level in both the I and Q channels. A sample is then recorded during a chosen period of time and a backup memory used to retrieve the initial part of the useful burst signal, existent before the threshold limit.

This backup memory records the last 0.5 ms of the input signal and adds that information to the sample when the event is recorded. The threshold level was set manually but it is only a function of the background noise. This should guarantee that a signal with its amplitude or intensity is due to a single particle-scattering and not due to a noise signal. The figure 15 shows an example of a burst signal from one channel, the threshold level used and the effect of the backup memory in the burst sample data.

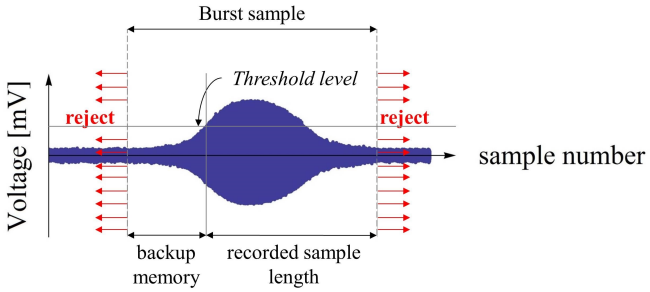

Figure 15: Threshold level, backup memory length and recorded sample length.

If the figure 15 is taken as example, the data reaches the computer from its left side. When the signal intensity matches the threshold level the sample starts being recorded during a predefined time length. The burst outset is retrieved by the backup memory that stores its information temporarily and every other noise data is rejected until a new burst triggers the recording system.

Possibly due to shot noise, some samples were triggered by a random momentary signal above the threshold level, presenting no useful data, as seen in figure 16.

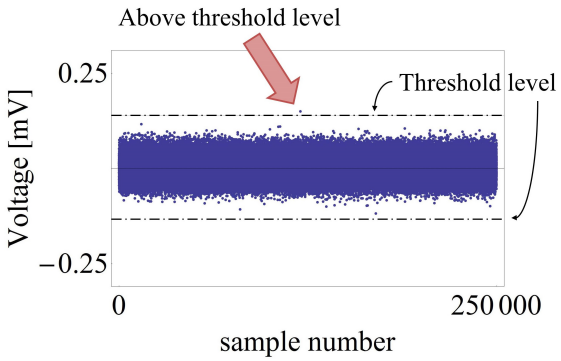

Figure 16: “Blank” sample due to false trigger caused by shot noise.

By imposing the threshold level trigger in both channels, the chance that shot noise would activate the data recording was decreased and these “blank” samples avoided.

2.2 Signal Processing

Once created, the data was imported and processed using Wolfram *Mathematica®*. The functions and codes used to export and analyze the calculated speed and accelerations are stated in section §7.2 while in this section only the algorithm or the computation steps are presented.

A test is defined as a collection of bursts samples during the moment the data is continuously recorded. Each burst sample is composed by two files, from the two input channels, which are expected to be almost identical beside the $\pi/2$ phase shift explained in section §2.1.1. The several Doppler frequency measurements will be referred as samples that should not be mistaken as "burst samples". These are recorded as a binary data series composed by the signal intensity, measured and amplified in mV, produced at the sampling rate selected over the chosen time sample. For both field and lab measurements a time sample of 3 ms showed to be enough to identify a full burst. The Nyquist-Shannon theorem states that an analog signal can be recreated from its sample values if the sampling rate is at least two times the highest frequency of the measured signal [15], while in practice a scale of 2.5 to 10 times the highest frequency is used [32]. For the carry out tests a sampling rate of 120 MHz was used and guarantees the minimum advised rate (2.5 times the measured frequency) for wind speeds until 37 m/s.

In order to categorize the different computing steps, these were itemized in the following way:

- Importing the data
- Locating and selecting the burst signal
- Filtering the signal
- Calculating the I/Q signal frequency variations
- Calculating speed and acceleration

For illustrative purposes a sample from an outdoor test was selected. The images presented consist in the representation and evolution of the signal for each step described.

2.2.1 Importing the data

The sample data is imported using a binary reader, converting its contents to an array of data where each row represents the intensity value of the signal. If plotted this array would look like figure 17 and its shape would resemble a Gaussian function by the reasons explained in section §1.4.

Since the selected sampling rate is too high to distinguish several evaluations in figure 17 with this scale, the figure 17 also represents what would it look like if the same signal was produced at a lower sampling rate (by a factor of 16).

At the bottom of the same it is also possible to distinguish the shape of a noise signal and a clear signal with useful information.

2.2.2 Locating and selecting the burst signal

Once the sample is bigger than the burst size and contain mostly noise outside its limits (see section §2.1.1 for noise details) it is necessary to isolate the section containing useful information.

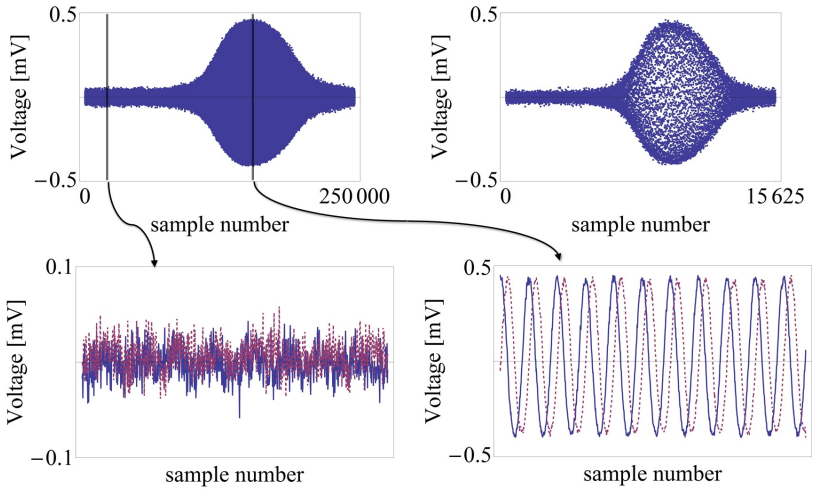

Figure 17: On top: Raw signal on the left and same signal if obtained at a lower sample frequency on the right. At the bottom: noise signal from both channels on the left, clear signal from both channels on the right. (Channel 1 - Thick line; Channel 2 - Dashed line) .

***LocateBurst* function** To locate the burst the variances of 10 µs partitions, corresponding to 1200 samples, of the first channel file from the sample, are analyzed. It is expected that for the noise sections, where its value is located in a small and relatively constant interval, its variance to be smaller than in sections where the signal presents marked variations as is the case of the burst. After selecting the partitions where its variance is higher than its third or upper quartile, the full width at half maximum (FWHM) is calculated. This in turn is connected to the standard deviation by the expression

$$\sigma = \frac{FWHM}{2\sqrt{2\ln(2)}} \tag{2.5}$$

that will be used as a bounding factor later [20]. The center of the burst (*cen* in figure 18) can be estimated either by the variance median or maximum position (only of the partitions selected as described). In this case the median criterion was used. The figure 18 illustrates the time partitions variance distribution and the pointed variables in the ***LocateBurst*** function.

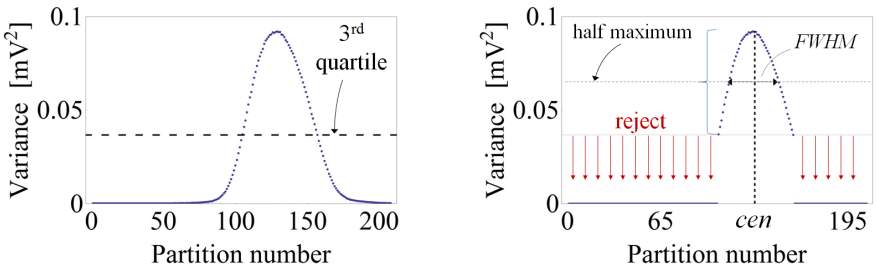

Figure 18: Time partitions variance distribution and variables in the ***LocateBurst*** function.

This function returns a vector with the location of the burst center and the standard deviation referred.

***TakeBurst* function** Given the center location and the standard deviation in (2.5) a portion of the whole sample is selected in order to isolate the burst for future analysis. For this purpose it was found that an interval of $\pm 3\,\sigma$ around the center could differentiate the intended boundary. Figure 19 shows the signal before and after using the *TakeBurst* function explained.

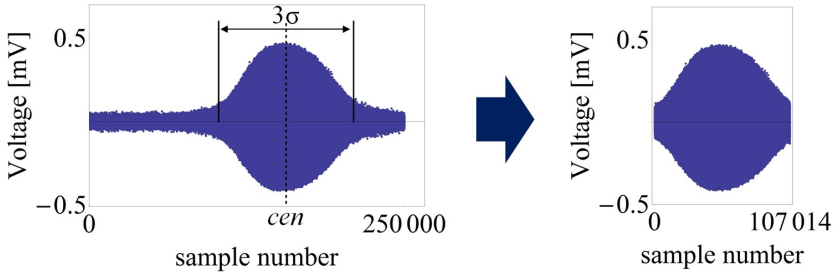

Figure 19: Signal before and after using the *TakeBurst*.

2.2.3 Filtering the signal

In order to get a good function fitting in section 2.2.5, to properly identify the flow speed and acceleration, the filtering function ***FilterBurst*** is applied. This aims to define and select only part of the waves that compose the signal by choosing the ones with frequencies close to the one from the wave with the highest amplitude.

In order to do this the first channel frequency spectrum is analyzed using a discrete Fourier transformation (DFT) and its main frequency location identified. The DFT transforms the data from time-domain to frequency-domain, converting an original data list into a new list of complex coefficients ordered by their frequencies.

Mathematica® default DFT definition is given by (2.6) where n is the list size, u_r the amplitude value of the original list and s the DFT list index

$$\mathscr{F}\{\mathbf{u}\} = v_s = \frac{1}{\sqrt{n}} \sum_{r=1}^{n} u_r \mathrm{e}^{2\pi \mathrm{i}(\mathrm{r}-1)(\mathrm{s}-1)/\mathrm{n}}\,,\ s = 1, 2, 3, ...n \tag{2.6}$$

and presents its output as a complex number. Each v_s is a result of a combination of integer multiples of a fundamental frequency given by $^{(s-1)}/_{n}$. After applying the DFT to the first channel signal, the frequency spectrum in figure 20 is then determined by its absolute square, and the frequency units presented in Hz.

The signal frequency with highest amplitude will be called the main frequency, and can be used to estimate the wind velocity by equation (1.30). The location of the main frequency (that corresponds to the s parameter) in the DFT list is then identified to be used in the filter function and will be labeled as s_0.

Afterward, a Gaussian distribution is created with an expected value equal to s_0 and a standard deviation as a function of a parameter named as *spectrum width*.

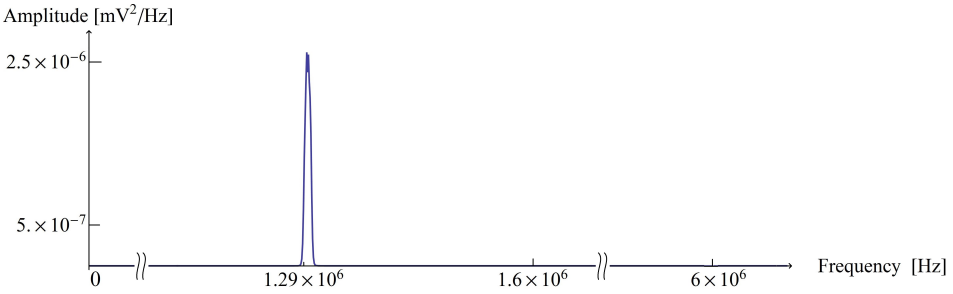

Figure 20: Channel 1 frequency spectrum.

Since the frequency spectrum has a narrow shape and is composed by discrete values it was shown to be hard to define a standard deviation according to (2.5). Instead of evaluating the FWHM as previously, a length measure (*spectrum width*) is defined as the full width at 1 % of the spectrum maximum. After applying a Fourier transformation to both channel signals and multiplying those by the filtering Gaussian distribution defined, the inverse Fourier transformation is calculated. With this the signal retrieved resembles the raw I/Q signal excluding some noise and unwanted fluctuations.

For the tests carried out, the standard deviation of the Gaussian function used for filtering the frequency spectrum was defined as two times the parameter *spectrum width.*

Figure 21 overlaps the signal DFT absolute square (from which the frequency spectrum is determined) peak with the filtering Gaussian function for three different standard deviations (0.05, 2 and 30 times the *spectrum width* parameter).

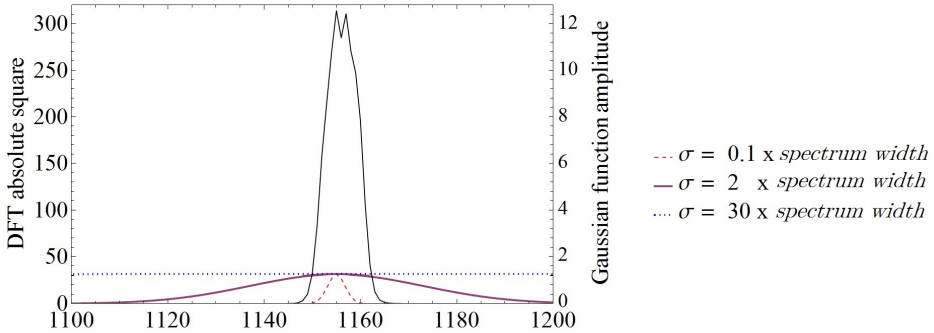

Figure 21: DFT absolute square and Gaussian filter function with different standard deviations.

If a small standard deviation is chosen it becomes impossible to determine the particle acceleration since this is related to changes into the Doppler shift frequency. This can be noticed by the fact that the Gaussian curve represented as a dashed line in figure 21 is too narrow and will attenuate some frequencies inside the frequency spectrum peak after being multiplied by the signal DFT. The opposite happens for too high standard deviations. In this case the Gaussian filtering curve does not fulfill its role to attenuate the noise frequencies outside the frequency peak and the final, speed and acceleration curve ,fitting in section 2.2.5 does not adjust properly to a linear function. Figure 22 shows the final result in the last computing step when using these same Gaussian function standard deviations and its consequences

in the final function fitting.

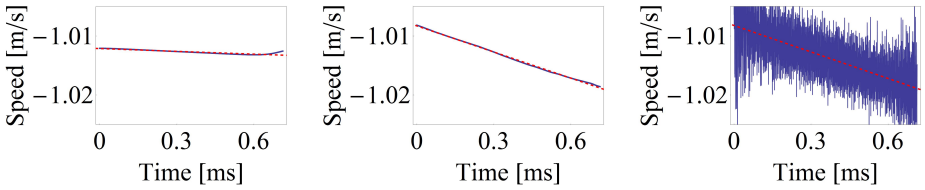

Figure 22: Final result with different Gaussian function standard deviations: 0.05 on the left, 2 at the center and 30 on the right (times the *filter width* parameter).

Correlation for future data validation As it will be explained in section 3.2.2 some defective signals can return unrealistic values, specially the ones regarding the wind acceleration. In this stage of the algorithm a signal property is evaluated so it can be used to qualify the burst signal and, if necessary, discard the respective sample from the test.

This is done in this stage of the algorithm, by evaluating the correlation between the absolute values of the filtered signal and a fitting Gaussian function obtained by the ***TakeBurst*** function already exposed.

Overlapping burst signals are expected to have a lower correlation factor than good signals. The figure 23 shows two examples of these cases. The one on the left as a correlation of 0.42 with its Gaussian fit, at the same time the bad signal on the right has a correlation factor around half of the value found for good signals. Please note that since the signal is periodic it is never expected the correlation value to be close to 1, but it was still found to be a good single-burst "quality" evaluation.

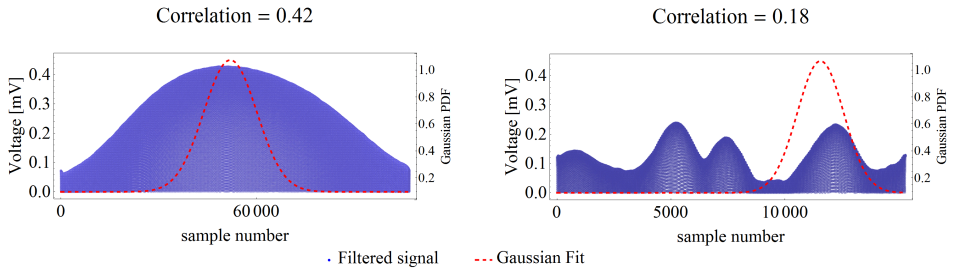

Figure 23: Correlation factor between the absolute filtered signal and a Gaussian fitting function.

2.2.4 Calculating the I/Q signal frequency variations

As mentioned in section §2.1.1 a simple in-phase/quadrature (I/Q) modulation is applied to the detected signal. Its demodulation allows the measurement of the amplitude, phase and instantaneous frequency, as well as its sign [13], inherent to the speed direction. A positive frequency sign is connected to a speed toward the instrument and vice versa. As previously mentioned, the channel 1 corresponds to the in-phase signal and the channel 2 to the quadrature.

A phasor can then be defined for each frequency that composes the sample and be represented in its complex form according to Euler's formula:

$$A\left(\cos(2\pi f\, t+\phi)+\mathrm{i}\sin(2\pi f\, t+\phi)\right)=A\mathrm{e}^{\mathrm{i}(2\pi \mathrm{f}\, \mathrm{t}+\phi)} \tag{2.7}$$

where A is the amplitude, f the frequency in Hz and ϕ an initial phase angle. In figure 24 an illustrative I/Q signal with a single frequency and constant amplitude is represented over time and on the right the phasor projection onto the complex plane.

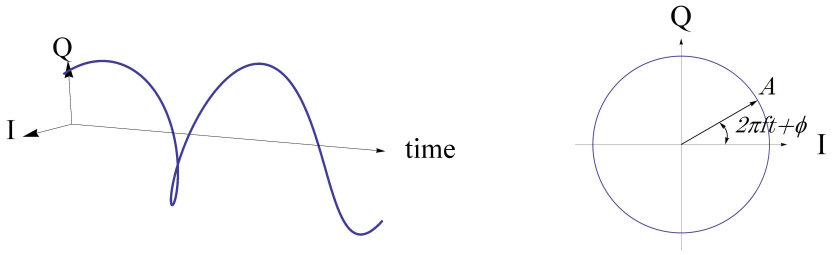

Figure 24: I/Q signal representation over time and its projection in the complex plane.

After filtering, the I/Q signal is still composed by multiple sinusoidal functions with different frequencies and amplitudes. If plotted on the complex plane they would resemble the representations in figure 25 where it also exhibit the effect of the filtering step in section 2.2.3.

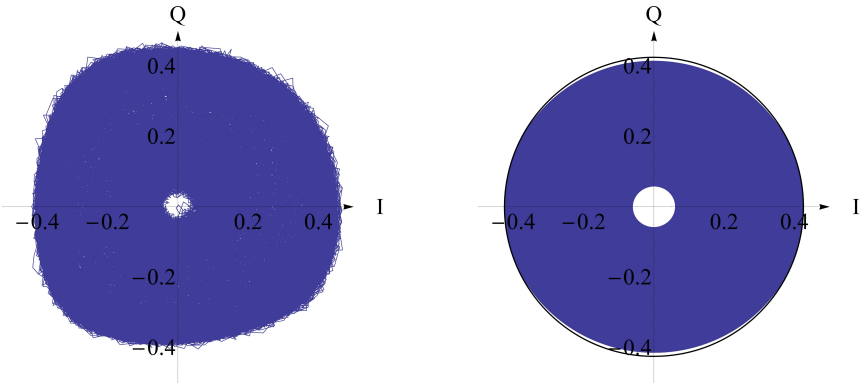

Figure 25: I/Q signals, before and after filtering, representation in the complex plane. Signal duration $\approx 0.9\,\mathrm{ms}$

If only, in this case, 0.8 µs were represented the result would be as the one in figure 26. (The value of 0.8 µs pretends to represent a single turn in the complex plane and can only be determined after evaluating the signal frequency)

Although it may not be easy to observe at the presented scale (in figure 25), the quadrature signal produced showed a slightly different amplification than the in-phase signal. A tangent circle to the I signal (with maximum amplitude) was added in figure 25 to show that the highest amplitudes in the I and Q signal do not agree. When calculated, the complex argument or phase given by

$$\theta=\arg[I+\mathrm{i}Q] \tag{2.8}$$

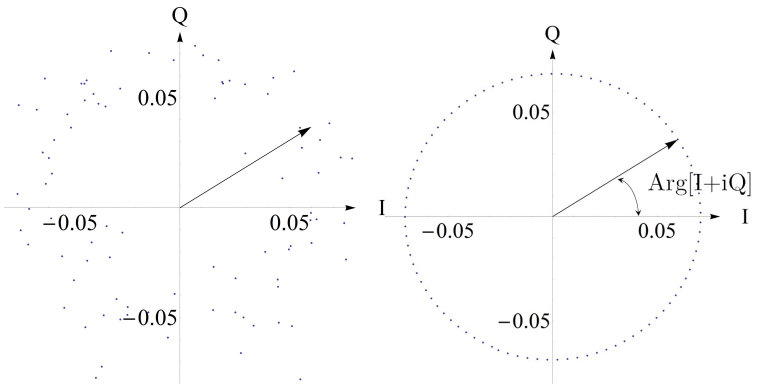

Figure 26: $0.8\mu s$ representation of the I/Q signal in the complex plane before and after filtering.

and the frequency given by (2.9) presented significant noise that could compromise the final result. The noise, due to imperfection in the quadrature signal, is not relevant to the phase determination and can be seen as small fluctuations in the phase function. Nevertheless, since the signal frequency is the phase time derivative, the noise effect becomes significant for its measurements.

To calculate the (Doppler) frequency, after dividing by 2π, a simple discrete differentiation is applied over each consecutive phase results.

$$f_D = \frac{1}{2\pi}\frac{\Delta\theta}{\Delta t} \tag{2.9}$$

In order to avoid the unwanted noise, a Hilbert transformation is applied to both channels and their final calculated frequencies averaged.

The Hilbert transform can be considered to be a filter which simply shifts phases of all frequency components of its input by $-\pi/2$ rad [6]. When calculated, this can replace the quadrature signal if the data from both channels is taken as the in-phase one independently. The continuous function is defined as in (2.10) although a discrete transform based on the routine in Marple's paper [16] was used.

$$\mathscr{H}\{y(t)\} = \frac{1}{\pi}\int_{-\infty}^{+\infty}\frac{y(\tau)}{t-\tau}\,\mathrm{d}\tau \tag{2.10}$$

The fast discrete Hilbert transform (DHT) algorithm used is unable to distinguish the frequency sign of the output signal. Due to this fact the phase between the two channels is also calculated in order to define the frequency sign and thus the flow direction. The discrete Hilbert transform (DHT) based on Marple's paper also showed to introduce some distortion if the input data is not perfectly periodic. For illustrative purpose a discrete cosine wave sample is shown in figure 27 as well as the result of its DHT. When the original sample last value is a multiple of its period (2π) the DHT presents a good approximation to a sine wave, while as expected but when it is not a multiple of the same a bad result is obtained.

The cosine waves in figure 27 were created from a discrete sample of values spaced by 0.1 radians. The one on top has values between 0 and 4π while the one at the bottom between 0 and 5π. The last presents a bad correlation with the expected sine wave and thus when applying the DHT algorithm to the I/Q signal a correction must be made.

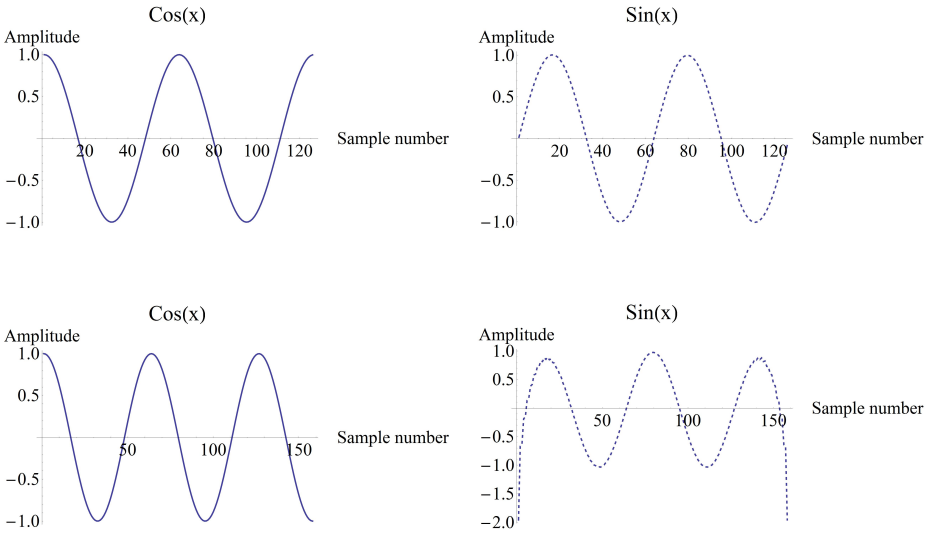

Figure 27: Discrete Hilbert transform of a discrete cosine function.

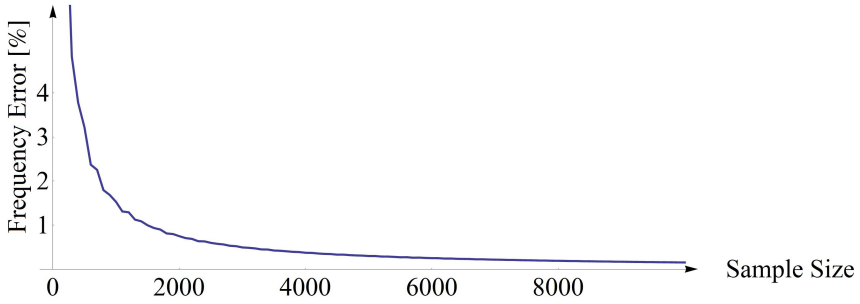

Figure 28: Frequency relative error *vs* sample size.

In order to determine the I/Q signal frequency, to infer about the flow speed and acceleration, its phase is determined, by simply evaluating the argument between both I and Q phasors that correspond to the same argument definition as in (2.7). Later this is accumulated over 2π intervals and discretely derived over time to calculate the signal frequency according to (2.9).

For this simulation, in what regards the frequency determination, it was also observed that the relative error between the real value and the one obtained from a "bad" DHT trend line decreases with the sample size. The frequency relative error was defined as the difference between the real and the determined signal frequency divided by the real signal frequency. For the previous illustrative case in figure 28 the frequency relative error is shown according to the sample size.

In order to avoid some errors the first and last 10% of the sample are trimmed after the DHT is calculated. This assures a better fitting function in section 2.2.5 and consequent speed and acceleration estimation.

2.2.5 Calculating speed and acceleration

After averaging the instantaneous frequency data from the two channels, both frequency and sample number were converted to speed (according to equation 1.30) and time domain related to the sample frequency. A linear regression is then performed, the velocity defined as its average value in the time selected, and the average acceleration as the linear regression slope. The figure 29 shows the final result: the frequency variations (small in this case), its trend line (dashed line) and velocity equation.

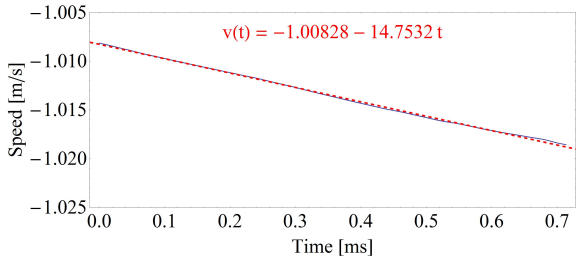

Figure 29: Speed and acceleration determined from the instantaneous frequency signal

2.2.6 Alternative solutions

An alternative Gaussian fitting function An alternative for the algorithm explained in section 2.2.2 was made taking advantage of the I/Q modulation properties. Although it has not been implemented due to its high memory demands and long evaluations it was found important to report it.

In order to use *Mathematica*'s built-in fitting functions, the raw signal had to be replaced by its envelope, *env*. The signal's envelope can be defined by

$$env\,(I, Q) = \mathrm{Abs}[I + \mathrm{i}Q] \tag{2.11}$$

After this, a Gaussian function is fitted to the data and returns a more accurate result than the ***LocateBurst*** function in section 2.2.2.

The figure 30 shows the I/Q signal envelope and both Gaussian fitting functions, either obtained by the parameters given by ***LocateBurst***, either by the alternative algorithm.

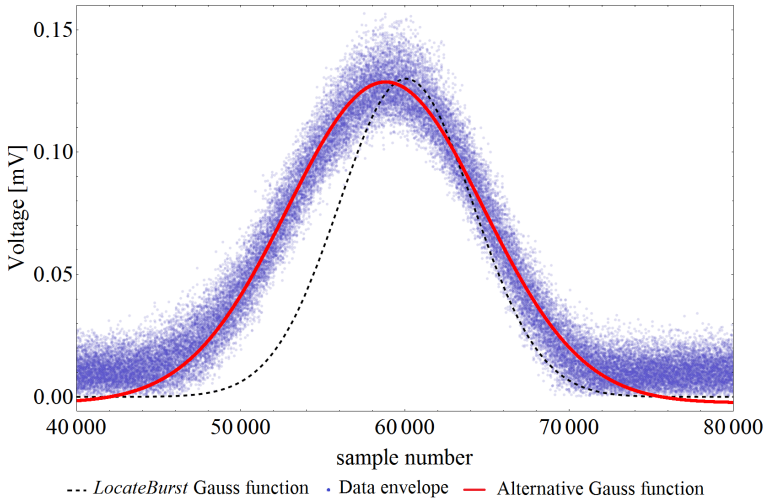

Figure 30: I/Q signal envelope and Gaussian fitting functions.

2.3 Radiation Pressure

In order to use the lidar technology to perform single-particle anemometry measurements, a short laser focus range must be used. This leads to a high laser power concentration in the probe volume that may interact with the measured particles.

In this section the effect of that light or radiation pressure is estimated in order to verify a possible interaction. The deduced expressions and models concern the case where the particle travels along the beam direction in the beam axis, where the effect should be strongest.

According to Maxwell treatise about electromagnetism, both electric and magnetic fields that compose radiation lead to mechanical stresses outside a surface element. The reaction force per unit area or radiation pressure can be deduced from the light (time-averaged) momentum density. Considering θ as the radiation incident angle in a surface, the momentum transfer can also be described as a resultant pressure in the same direction as the radiation, considering both absorption and reflection of the same[3] [17]. The equations (2.12) and (2.13) describe that pressure for both cases:

$$P_{abs} = \frac{\langle \mathbf{S} \rangle}{c} \cos\theta \tag{2.12}$$

$$P_{ref} = \frac{2\langle \mathbf{S} \rangle}{c} \cos^2\theta \tag{2.13}$$

where $\boldsymbol{S}$ is the Poynting vector that represents the energy flux density (Wm^{-2}), and comprises both electric and magnetic fields in radiation, and c is the speed of light.

[3]There is also a pressure due to the emitted radiation from a body surface. This will be ignored in a posterior analysis since it is centripetal for spherical particles and doesn't affect its motion. In fact the radiation is nether totally absorbed nor totally reflected, and even its reflection can be spread in all directions depending upon the surface optical properties.

Considering a spherical particle and a Gaussian beam irradiance, as the energy flux density in the particle surface, the Newton's Second Law of motion gives the acceleration transmitted to the particle due to radiation pressure:

$$\Sigma \mathbf{F} = \dot{\mathbf{Q}} = m\mathbf{a} \tag{2.14}$$

Once the irradiance is a function of the radial distance to the beam center axis it also has to be integrated along the surface area. The figure 31 illustrates some geometrical considerations taken into account.

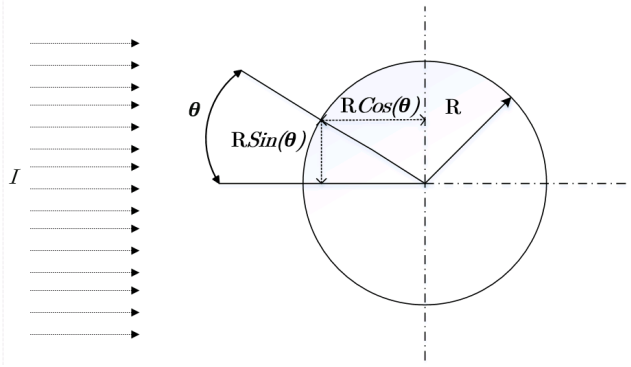

Figure 31: Geometrical consideration taken in integrals along the particle surface.

Solving (2.14) for the acceleration in the beam axis direction and considering the radiation pressure as the only force distribution in the particle (in the radiation direction) it returns:

$$a = \frac{1}{m} \int_{-\pi/2}^{\pi/2} P(\theta) \pi R^2 \cos\theta \, \mathrm{d}\theta \tag{2.15}$$

2.3.1 Model for Radiation Absorption

Considering the equations (1.37), (2.12) and (2.15):

$$a_{abs} = \frac{\pi R^2}{m} I_0 \left(\frac{w_0}{w}\right)^2 \int_{-\pi/2}^{\pi/2} \exp\left(\frac{-2R^2 \sin^2\theta}{w^2}\right) \cos^2\theta \, \mathrm{d}\theta \tag{2.16}$$

and since for an homogeneous sphere its mass can be defined as

$$m = \frac{4\rho\pi R^3}{3} \tag{2.17}$$

replacing (2.17) and (1.37) in (2.16) and solving the integral it returns:

$$a_{abs} = \frac{3P_0}{4\rho\pi R c w^2} \exp\left(\frac{-R^2}{w^2}\right) \pi \left(\mathcal{I}_0\left(\frac{R^2}{w^2}\right) + \mathcal{I}_1\left(\frac{-R^2}{w^2}\right)\right) \tag{2.18}$$

where $\mathcal{I}_n(z)$ gives the modified Bessel function of the first kind that is defined as

$$\mathcal{I}_n(z) = \frac{1}{2\pi \mathrm{i}} \oint \exp\left(\frac{z}{2}\frac{(t+1)}{t}\right) t^{-n-1} \, \mathrm{d}t \tag{2.19}$$

2.3.2 Model for Radiation Reflection

Through an analogous method to the previous, the acceleration for reflection case can be given by

$$a_{ref} = \frac{2\pi R^2}{m} I_0 \left(\frac{w_0}{w}\right)^2 \int_{-\pi/2}^{\pi/2} \exp\left(\frac{-2R^2 \sin^2\theta}{w^2}\right) \cos^3\theta \, \mathrm{d}\theta \tag{2.20}$$

that after taking some steps as previously and solving the integral, the following result is achieved:

$$a_{ref} = \frac{3P_0}{\rho\pi R c w^2} \frac{4\,\frac{R}{w} \exp\left(-2\frac{R^2}{w^2}\right) + (-1 + 4\frac{R^2}{w^2})\sqrt{2\pi}\,\mathrm{erf}\left(\sqrt{2}\left(\frac{R}{w}\right)\right)}{8\left(\frac{R}{w}\right)^3} \tag{2.21}$$

where $\mathrm{erf}(x)$ is the Gauss error function defined in (2.22)

$$\mathrm{erf}(x) = \frac{2}{\sqrt{\pi}} \int_0^x \exp\left(-t^2\right) \, \mathrm{d}t \tag{2.22}$$

Considering a particle with the same density as water it is possible to compare the predicted acceleration based in both models described. The results are shown in figure 32 as a function of the particle radius for a laser power $P_0 = 1\,\mathrm{W}$.

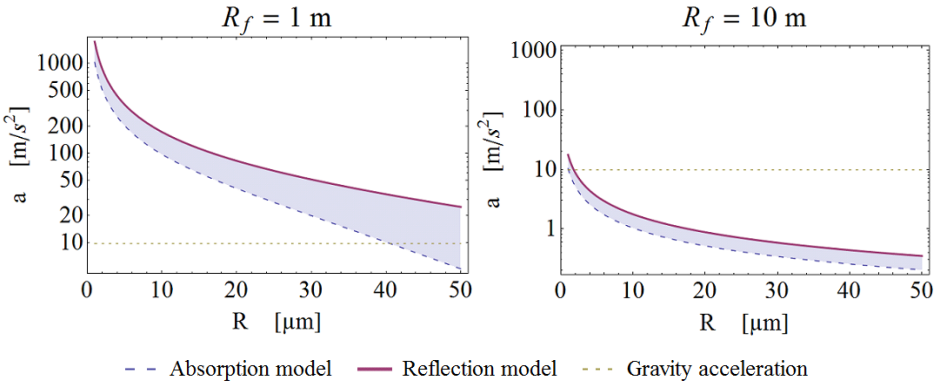

Figure 32: Acceleration due to radiation pressure for different particle sizes and beam focus distances.

2.3.3 Mean acceleration through the probe volume

The figure 32 shows the maximum predicted acceleration due to light pressure that occurs in the center of the beam in its waist. Due to its small dimensions the moment when that acceleration acts in the measured particle is also small, depending on the particle size, speed and direction and the beam geometrical characteristics.

Numerical averaging of the acceleration along the beam center shows that within the volume delimited by the Rayleigh length z_R its value has still the same order of magnitude of the maximum acceleration for both models described in 2.3.1 and 2.3.2 for any focus range whatsoever

$$\langle a(R) \rangle = \frac{\int_{-z_R}^{z_R} a \, \mathrm{d}z}{\int_{-z_R}^{z_R} \mathrm{d}z} \approxeq 0.8 \, a_{w_0}(R)$$

where $a_{w_0}(R)$ is the acceleration in the beam waist represented in figure 32.

Although the bursts length observed from the lidar signal are related to a smaller distance than z_R, the particle's trajectory along the measurement volume seldom agrees with the beam axis and therefore the experienced and measured acceleration are not expected to coincide with the predicted values. In fact as it was mentioned in section §1.4 the particle crosses the probe volume in trajectories close to the transverse direction.

Chapter 3

3 Measurements, Results and Discussion

3.1 Laboratory tests

3.1.1 Test description and results

In order to validate the technique and algorithm used to detect particles acceleration a lab test was executed. The test consisted in several measurements of a component of the centripetal acceleration suffered by a target attached to a spinning wheel. The last had a 300 ± 0.01 mm radius and a radial run-out (or oscillation) of ± 0.015 mm. The target used to intercept the lidar beam was a needle with a maximum diameter of 0.6 mm, fixed to the wheel using duct tape as shown in figure 33.

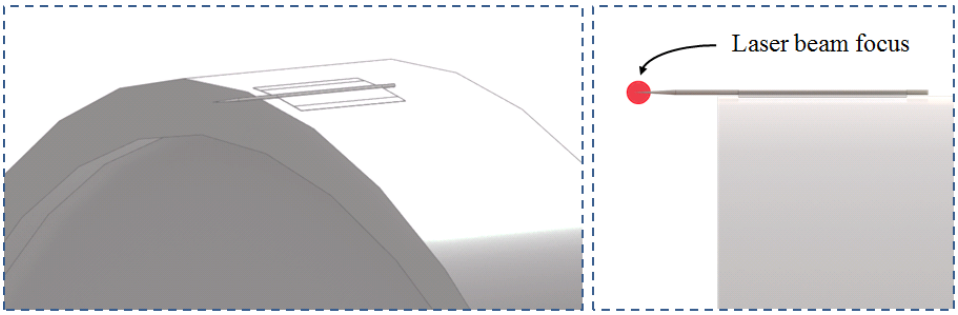

Figure 33: Needle detail in the spinning wheel and laser focus position.

If the lidar is focused on the top of the wheel with an angle α, as shown in figure 34, the measured speed by the lidar is equivalent to $v_t \cos(\alpha)$, where v_t is the tangential speed at the mentioned point. In a similar way, it is expected that the measured acceleration would relate to $a_c \sin(\alpha)$, where a_c is the centripetal acceleration suffered by the needle. Please note that the angle α is small and may mislead into interpreting that the beam was shot tangent to the wheel. Although the needle crosses the laser beam in two different locations, in only do it inside the probe volume in one point. This guarantees that all the speed and acceleration measurements concern the same location on the wheel.

The tangential speed can be given by (3.1) and relates to the centripetal acceleration by (3.2)

$$v_t = \frac{\Omega 2\pi R}{60} \tag{3.1}$$

$$a_c = \frac{v_t^2}{R} \tag{3.2}$$

where R represents the distance between the needle and the rotation axis and Ω the wheel angular speed in rpm.

In order to aim the lidar beam focus in the needle tip an oscilloscope was used. The focus can be roughly set into the needle position using an infra-red reflective paper, but a continuous visualization of the scattered signal improves the accuracy.

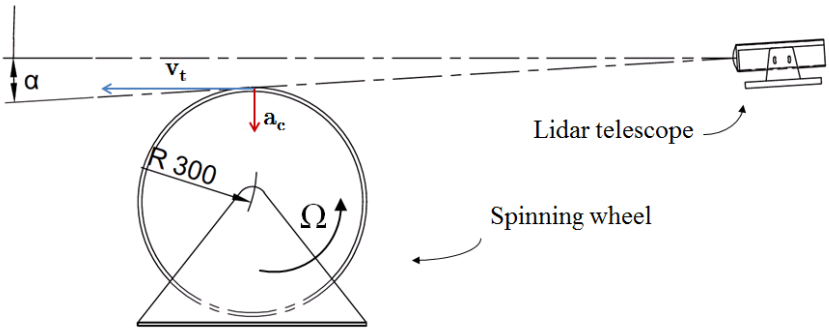

Figure 34: Needle tangential speed and centripetal acceleration.

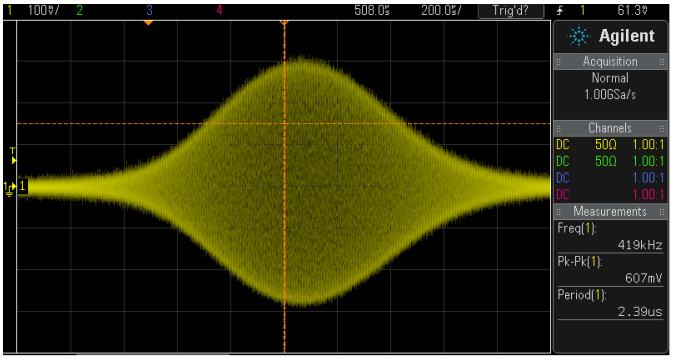

Figure 35: Observed signal in he oscilloscope due to the needle movement.

The figure 35 shows the observed signal in the oscilloscope before it was sent to the computer for recording.

The motor connected to the wheel was set to an angular speed of 600 ±0.03 % rpm for 30 s and then turned off allowing friction to slowly decrease the wheel rotation. The total duration of the test was roughly 3 min.

Since the wheel is also decelerating the unsteady acceleration must be taken into account. In this case, it was found that its value was significantly inferior compared to the centripetal acceleration and therefore discarded. The unsteady acceleration was determined by the time derivative of a polynomial fitting function done to the speed measurements. The figure 36 shows the speed measurements, their fitting curve and the determined unsteady acceleration.

The constant speed step was used to determine the angle α by considering the speed measurements accurate, averaging them and comparing it with the expected speed. Therefore α is calculated according to

$$\alpha = \arccos\left(\frac{\langle v \rangle}{v_t}\right) \tag{3.3}$$

Besides the resolution in the measured acceleration explained in section 3.1.2, other factors contributing to the measurements uncertainty are associated with the wheel angular speed, its radius, the existence of oscillations in the movement, the needle position and alignment and with the laser focus position. These have a strong influence in the measured and expected acceleration values. The figure 37

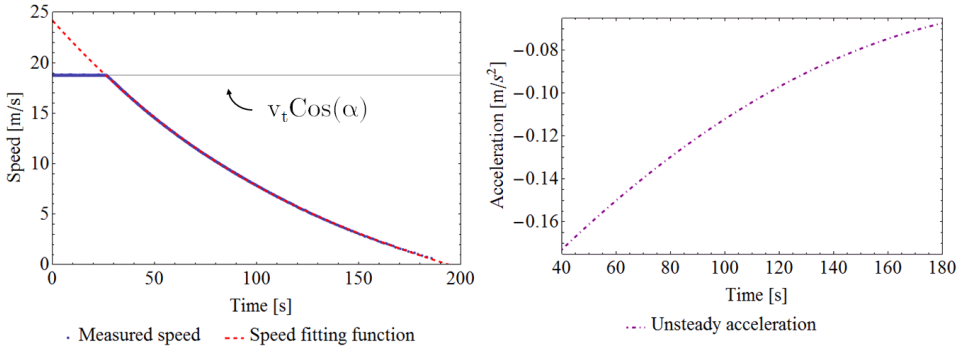

Figure 36: Speed measurements, speed fitting function and unsteady acceleration.

shows the expected acceleration determined by (3.2) and the measured values on the left, and the same on the right if a tolerance of $-1°$ is given to α.

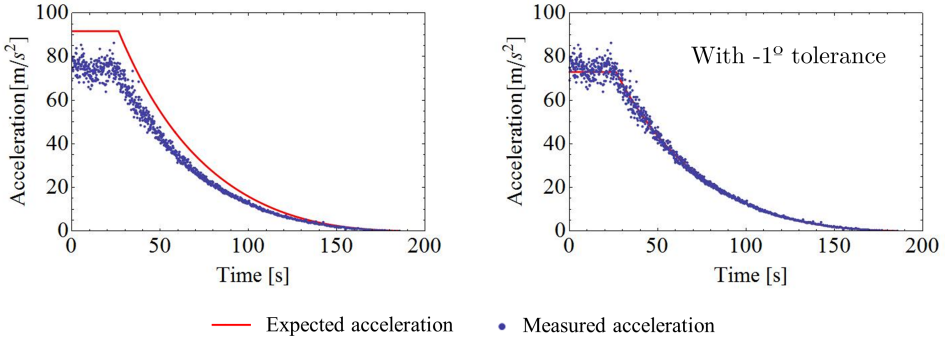

Figure 37: Expected and measured acceleration on the left, and the same with a $-1°$ tolerance in the α angle.

Due to difficulty in determining all the uncertainties propagation of the instruments, the figure 38 also shows the expected acceleration boundaries if the wheel radius is relaxed with a ± 0.5 mm uncertainty.

As the figure 38 supports, the measured and expected acceleration values are highly sensitive to the parameters uncertainties as referred, but do present a strong correlation between each other, and in this case equal to 0.995, what suggests a proper technique and evaluation algorithm.

3.1.2 Measured acceleration resolution and uncertainty

Expected acceleration uncertainty Although it was shown to be hard to measure the uncertainties associated to the different elements in the experiment setup as said, the accuracy in the acceleration determination can be estimated.

If the algorithm in section §2.2 is taken, the wind acceleration is calculated based on the slope of a linear fitting function done to the speed changes over the burst time length. Therefore it can be said that

$$a = \frac{\Delta v}{\Delta t} \tag{3.4}$$

where Δv represents the speed change over the burst and Δt the burst duration.

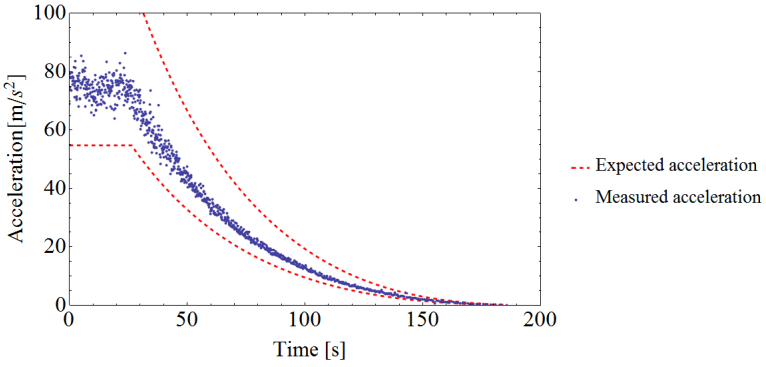

Figure 38: Acceleration measurements and theoretical boundaries if a $\pm 0.5\,\text{mm}$ uncertainty is given to the wheel radius.

An uncertainty propagation analysis states that

$$\frac{\sigma\left(a\right)^2}{a^2} = \left(\frac{\sigma\left(\Delta v\right)^2}{\Delta v}\right)^2 + \left(\frac{\sigma\left(\Delta t\right)^2}{\Delta t}\right)^2 \tag{3.5}$$

where $\sigma\left(a\right)$, $\sigma\left(\Delta v\right)$ and $\sigma\left(\Delta t\right)$ represent the acceleration, velocity and duration absolute uncertainties respectively [2].

Since Δt is only a function of the burst sample length and the sampling rate, it was considered that its uncertainty is null.

Therefore, by simplifying (3.5), $\sigma\left(a\right)$ is defined as

$$\sigma\left(a\right) = \frac{1}{\Delta t}\sigma\left(\Delta v\right) \tag{3.6}$$

If equation (1.30) is considered, $\sigma\left(\Delta v\right)$ can be rewritten as $\sigma(\Delta v) = \lambda/2\,\sigma(f_D)$ where $\sigma\left(f_D\right)$ can be associated with half the resolution in the frequency spectrum provided by the signal DFT. Although this consideration may be somehow conservative, it can be considered as an upper bound estimation of the speed or frequency uncertainties. This (frequency resolution) in turn can be defined as $120\times10^6/n$ as exposed in (2.6) and the time duration can be defined as $\Delta t = n/\left(120 \times 10^6\right)$, where n represents the burst sample length or the total number of Doppler frequency evaluations in the considered signal.

If the sampling rate, the lidar wavelength, and the burst sample length are certain, the expected acceleration absolute uncertainty can be defined only as a function of n as in

$$\sigma\left(a\right) = \frac{\lambda \times 120 \times 10^6}{4n^2} = \frac{5.634 \times 10^9}{n^2} \tag{3.7}$$

for the lidar wavelength and sampling rate used.

Measured acceleration uncertainty In order to measure an estimate of the acceleration uncertainty several tests executed as in section 3.1.1 were performed with different angular speeds Ω and angles α.

In this case, for each configuration, distinct acceleration measurements were done, sorted in groups with common parameters (Ω and α), and their standard deviation, $\left\langle a^2\right\rangle^{1/2}$, evaluated as well as the mean sample size of the respective signals.

The acceleration measurements uncertainties can be defined using a Student's t-distribution [2]. For a 95 % confidence interval this is equal to

$$\sigma(a) = t_{95\%} \left\langle a^2 \right\rangle^{1/2} \tag{3.8}$$

where $t_{95\%}$ is the t-value for a two-tailed distribution which is only a function of the degrees of freedom of the acceleration sample groups formed. These degrees of freedom are equal to the group size minus one.

The figure 39 shows the measured acceleration uncertainties according to (3.8) and the predicted values according to (3.7) as a function of the burst sample length.

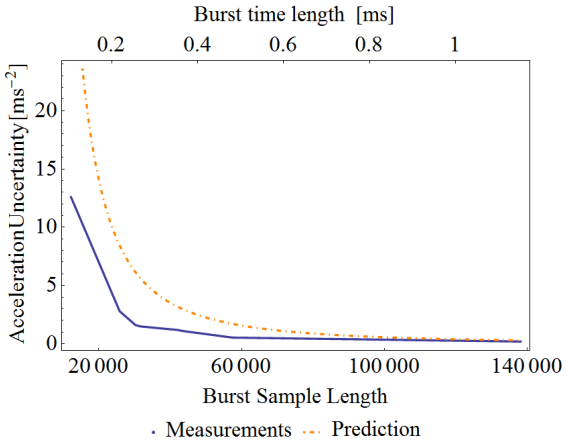

Figure 39: Acceleration absolute uncertainties: measurements and prediction.

As it is observed, the accuracy in the acceleration measurements with this technique is highly sensitive to the burst sample size, introducing significant errors in short signals. If the predictions from equation (3.7) are correct, signals with a time length < 0.2 ms can introduce errors or uncertainties in the measurements in the order of $\backsim 10\,\mathrm{m/s^2}$.

The figure 40 shows the results from another test. In it is represented the acceleration measurements, the theoretical or predicted acceleration and the uncertainty boundaries determined by adding and subtracting, to the predicted acceleration values, the absolute uncertainty evaluated through (3.7).

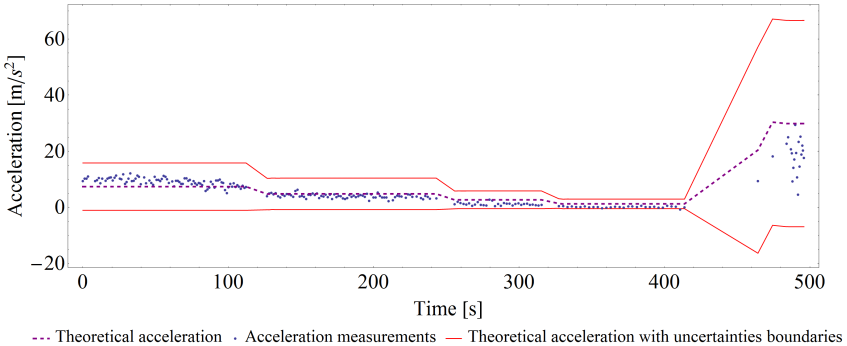

Figure 40: Acceleration measurements, theoretical acceleration and uncertainty boundaries.

3.2 Technical limitations

In this section some uncovered problems and limitations of the lidar, data acquisition system, and data processing are described. They can lead to unwanted influences in the flow speed and acceleration determination either by constant disturbance (section 3.2.1) or by improper data acquisition or processing.

3.2.1 The effect of radiation pressure on acceleration measurements and statistics

As it was exposed in section §2.3 it is possible for the laser beam to affect the acceleration measurement results due to radiation pressure.

The radiation pressure models done in section §2.3 were developed for the strongest interaction from the laser with the measuring particles or, in other words, for the case where particles intersect the exact beam waist. Nevertheless, it was found important to evaluate such influence in real measurements although the particle seldom agrees with the "upper bound" conditions taken into account.

In order to evaluate the significance of the laser beam effect on the measurements three tests under similar conditions were made. These tests were done in a Risø lab, using a fan with constant speed to produce an air flow and a "disco" smoke can spray to artificially produce an aerosol. This last was required due to shortage of particles in the lab air (possibly caused by the air conditioning system). The laser beam was shot upstream in the direction of the lidar telescope, the focus range set to 1.2 m (to enhance the radiation pressure effect) and the bursts samples recorded during 40 min tests.

Although the air flow is turbulent, it is expected that, in the absence of any external force in the flow direction, the mean and median acceleration from each test results to be close to zero (see section 1.2.5). Due to turbulence randomness and test imperfections, such as superposition of bursts in the same sample or incomplete signals like the ones exposed in section 3.2.2, some extreme acceleration values were obtained. The acceleration mean can then be more affected by these values than the median, and thus the second was used for comparison.

The expressions (2.18) and (2.21) present the relationship between the acceleration caused by this effect and the particles and laser properties. From all the possible parameters, due to simplicity and to the direct relation between the acceleration and the beam power, this was used as the tests variable or conditional factor.

By using three different laser powers (360 mW, 470 mW and 950 mW) it was expected to observe three different deviations from the acceleration median to the zero value.

Since the signal from a single particle is emitted during a short period of time (~ 0.1 ms to ~ 1 ms) the predicted radiation pressure is not expected to affect the speed measurements and statistics, but only to influence the acceleration. Figure 41 shows the final speed and acceleration histograms for the different performed tests.

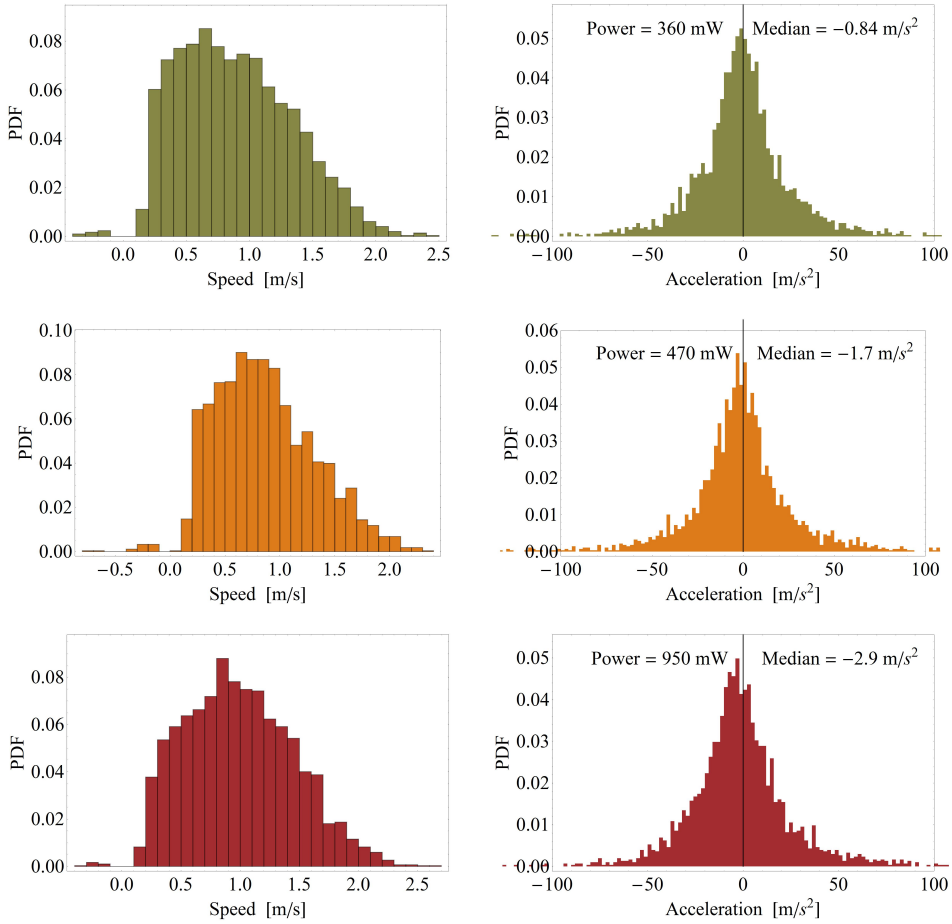

Figure 41: Speed and acceleration histograms for the measurements with three different laser powers.

As it is shown, for the three performed tests, the acceleration histograms show the previously described deviation. The median accelerations revealed to be different from zero and negative which mean that particles accelerated in the same direction as the beam and against the flow as predicted. It can be concluded then that for high laser powers and short focus ranges the acceleration statistics are significantly affected by radiation pressure. It can be avoided or reduced by using lower laser power and higher focus ranges.

3.2.2 Extreme acceleration or defective signals

When looking at the acceleration histograms, some of the measurements presented extreme values possibly related to imperfections or technological limitations. Since the algorithm in section §2.2 ran automatically through all the data it was impossible to discard automatically those "bad" samples that influence the acceleration statistics. When a closer look was taken through the burst samples, the "bad" ones were found to appear seldom, and although their contribution is relatively small within a test, it was found important to document them.

The "blank" samples as previously referred in section 2.1.2 contribute to null acceleration values and were fixed by implementing the trigger function in both the

I and Q channels as described.

Three other types of "bad" samples were also identified and are reported here.

Please note that "incorrect speed and acceleration determination" does not necessarily mean that in all those cases these values do not correspond to the expected, but that they add unwanted noise that can compromise the results.

Figure 42 pretends to represent how the acceleration histogram for the strongest laser power (950 mW) in figure 41 would look if plotted completely.

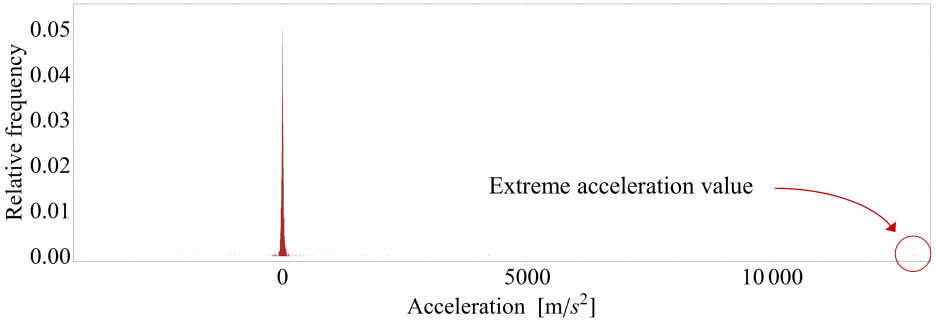

Figure 42: Whole acceleration histogram with extreme acceleration values

The extreme acceleration value (12 878 m/s^2) was determined by the signal with the shape presented in figure 43 that can be related to both overlapped signals and incomplete bursts.

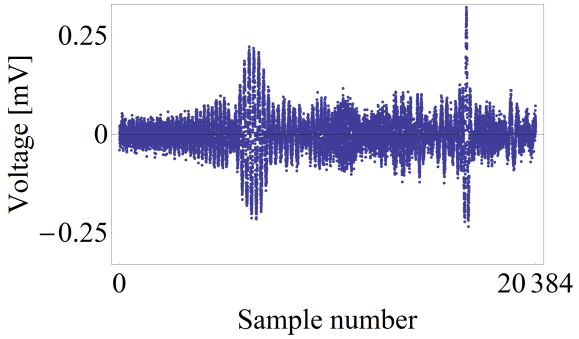

Figure 43: Signal responsible for extreme acceleration.

Signal saturation One first limitation is directly related to the hardware. In the ADC the electric signal is supposed to be limited to around 0.5 mV and experimental tests shown the value to be 0.56 mV. This limitation can lead to a signal saturation specially in cases where the backscattered intensity is high. This can be due to a high laser power, short focus ranges, big aerosol particles or to a high LO amplitude in the attenuator (see section 2.1.1) since it works as an optic amplifier.

Saturated signals were found in the lab tests presented in section 3.2.1 where these three conditions occur. The figure 44 shows a selected burst signal, the saturation limit (dashed lines) and the expected shape (dotted-dashed curves). Although the useful information is related to the signal frequency and not to its amplitude, in some cases the evaluation of the speed and acceleration from the signal frequency variation over time may have an additional error.

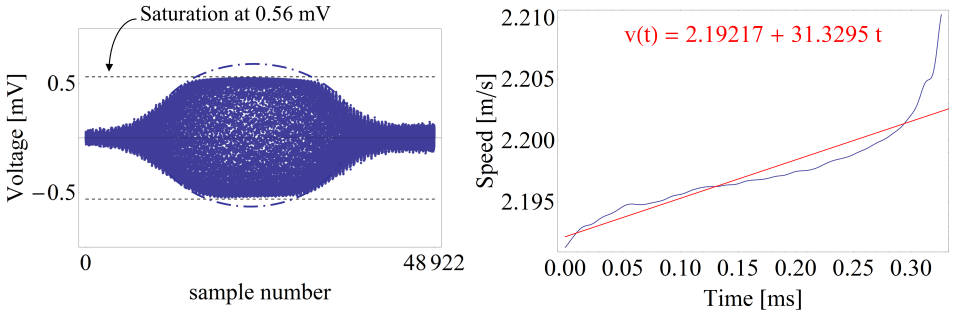

Figure 44: Saturated burst signal signal; saturation limit (dashed lines) and expected burst contour (dashed-dotted curves)

Overlapped signals Overlapped signals occur due to bursts superposition in the same measurement sample. This can happen if the threshold in the data acquisition system (section 2.1.2) is too low, the focus range small or if the particles density in the air is too high. As explained in section 1.3.3 the backscattered signal can also be composed by different particles contribution weighted by a Lorentzian function. In the presence of several particles in the measurement volume, the produced signals can overlap and lead to incorrect results. The determined acceleration is not the real acceleration, but merely a measure of the difference in velocity of two particles that happen to be in the same volume almost simultaneously.

Figure 45 presents an example of the overlapped signals and its effect in the speed and acceleration determination.

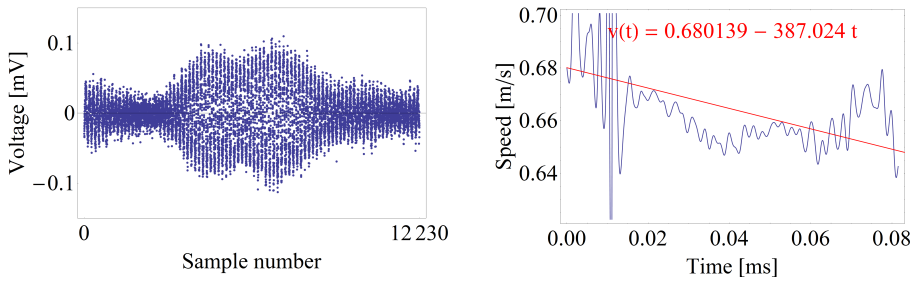

Figure 45: Overlapped bursts signal on the left and its consequence in the speed and acceleration determination

Incomplete bursts Some burst samples associated to high acceleration values presented a typical shape like the one in figure 46. Although its cause is not certain the fact that they are composed by overlapping bursts would imply that those occur in a way shorter period of time than expected. In other words, it was found unlikely that too many particles would cross the probe volume at the same time, generating the described signal shape. As earlier reported typical burst signals were found to take place between ~ 0.1 ms and ~ 1 ms. If the one presented in figure 46 was constituted by several smaller burst their time scale would require to be ~ 10 times smaller.

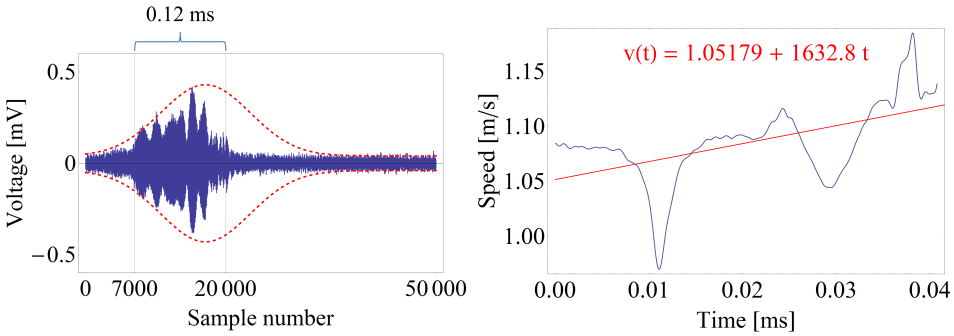

Figure 46: Incomplete burst signal and its consequence in the speed and acceleration determination

The fact that the signal amplitude increases over time suggest, as a theory, that the laser may interact with the particles at the point that it divides them into smaller fragments preventing a full burst to take shape. In figure 46 a Gaussian burst shape represented as a dashed curve, with a typical time scale, was superimposed to the real data in order to support this observation.

These burst samples seldom occur and may be related to cases where particles cross sections close to the beam waist. This effect can also be prevented or reduced by using lower laser powers and higher focus ranges.

3.3 Measurements of the universal constant a_0

In this section the executed field experiments are described and their results presented. The universal constant a_0 is calculated using (1.28) , by measuring $\langle a^2 \rangle$ using the lidar data and ϵ with a sonic anemometer, through the properties of the energy spectrum in the inertial subrange. The air kinematic viscosity ν was consulted in the *EES* (Engineering Equation Solver) database using the atmospheric pressure (101.325 kPa) and the flow mean temperature also measured by the sonic anemometer. The expression (1.28) can be rewritten as

$$a_0 = \frac{\langle a^2 \rangle}{\epsilon^{3/2} \nu^{-1/2}} \tag{3.9}$$

The experiments consisted in measuring the wind turbulent acceleration, with the lidar in the same region as the sonic anemometer evaluates the wind velocity. This was done by setting the lidar beam focus inside the sonic anemometer probe volume as shown in figure 47 and figure 48 at, approximately, 1.3 m height. The experiments were done in clear days with mean wind speeds above 3 m/s, usually from northwest, and during a period of approximately 3 h each. The wind velocity and turbulent acceleration component are determined in the lidar beam direction pointed upstream with a focus range of approximately 2.5 m.

For illustrative purposes, the images and plots presented in section 3.3.1 and section 3.3.2 relate to the same experiment that occurred on May 23^{rd} 2014.

3.3.1 Sonic anemometry results

The sonic anemometer used was a Campbell scientific CSAT3 sonic with three paths, slanted 30° from the vertical and in the azimuthal direction, equally spaced by 120°. The CSAT3 was used to determine the turbulent energy dissipation rate,

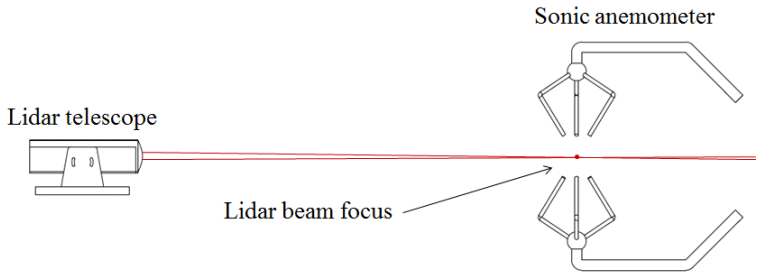

Figure 47: Lidar telescope and sonic anemometer setup.

Figure 48: Sonic anemometer and lidar telescope positioning in a field experiment.

as said, and to characterize the flow by defining its turbulent scales and Reynolds number.

The data comes as an array that returns a time stamp, the wind velocity components in a fixed orthogonal coordinate system and the fluid temperature. The reference coordinate system is characteristic of the sonic model and it was not aligned with the lidar beam. Nevertheless, the z direction is considered to be vertical and therefore always transverse to the wind flow.

After selecting the data corresponding the experiment time period, the energy spectra were determined. Since the wind flow direction is not constant over time it becomes harder to define the longitudinal energy spectrum rather than the transverse if the vertical direction is used. With this, the wind stream is being assumed to be parallel to the surface and the vertical mean wind speed equal to 0.

The energy spectra can be determined by (1.23) and each frequency converted to its respective wavenumber according to

$$\kappa = \frac{2\pi}{u_0} f \tag{3.10}$$

where f is the frequency of the DFT and u_0 the mean wind speed.

Figure 49 shows the longitudinal energy spectrum on the left and the transverse one on the right.

Both spectra presented the expected shape, similar to the one exposed in figure 2, for the inertial subrange. Nevertheless, a tangent line to the inertial subrange in a log-log scale representation of the spectra did not show, at first, the -5/3 slope as foreseen. This feature is due to the spatial averaging done by the sonic anemometer in its probe volume (with a 11.5 cm long path) by attenuating

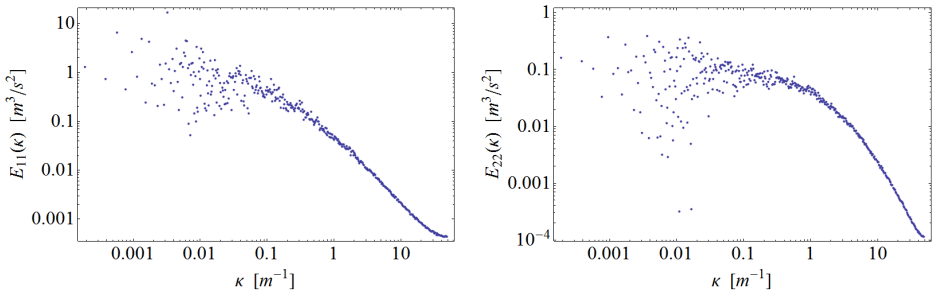

Figure 49: Energy spectra in the longitudinal and transverse direction ($23^{rd}$of May).

spatial variations that have wavelengths on the order of and shorter than the path length ($\kappa \gtrsim 8.7\,\mathrm{m}^{-1}$ for the equipment used) [10]. The noise in the spectra for high wavenumbers is also considered to be smaller in the vertical/transverse spectrum rather than in a horizontal direction, due to the sonic geometry and path averaging.

In order to correct this, an algorithm based on a paper by Horst and Oncley [10] was applied to the transverse spectrum. The figure 50 shows the exposed attenuation for high wavenumbers and the -5/3 slope tangent function.

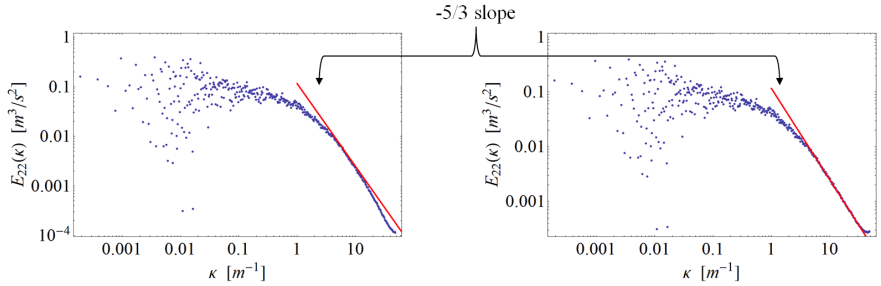

Figure 50: Transverse energy spectrum without and with path averaging correction ($23^{rd}$of May).

After fitting a tangent with a -5/3 slope to the inertial subrange, the energy dissipation rate ϵ can be determined according to equation 6 since the fitting function behaves as $E(\kappa) = C_k \epsilon^{2/3} \kappa^{-5/3}$ and $C_k = 1.5$ as previously stated.

For this experiment, ϵ was found to be equal to $0.21\,\mathrm{m}^2/\mathrm{s}^3$.

The u_{rms}, determined according to (1.5), can be used to define the Taylor's microscale λ through equation (1.8) and the Reynolds number associated to it through (1.9). The calculated values are defined in table 1 in the end of the present section for two different experiences.

The functions used to define the energy spectra can be found in section §7.2 as ***EnergySpectrum*** and ***EnergySpectrumPlot***.

Please note that the last returns a plot where the energy spectrum, in the ordinate, comes premultiplied by the wavenumber κ as it is common in some literature. In this case the plot in the inertial subrange follows a -2/3 instead of -5/3 power law. When applied to the vertical data of the sonic anemometer it allows the direct determination of the energy dissipation rate as shown in figure 51.

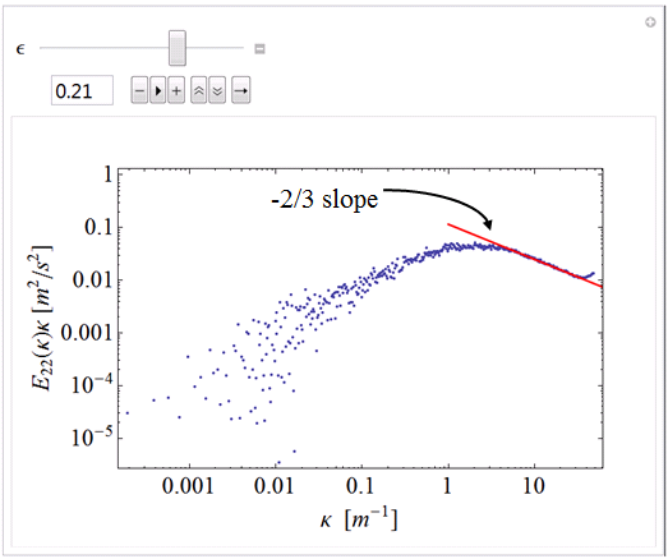

Figure 51: Direct determination of ϵ from $E_{22}(\kappa)\kappa$ ($23^{rd}$of May).

3.3.2 Lidar anemometry results

After recording and processing all the lidar data according to the algorithm explained in section §2.2, the final result is exported as an array with:

- The burst sample/identification number
- The wind speed
- The wind acceleration
- The correlation factor for filtering/validation (section 2.2.3)
- The burst sample length

This array allows the results to be exported to an external text file, for example, and processed with any other software rather than *Mathematica* if necessary.

The results array was then subjected to a filtering function to reject invalid results. This is done by calling the ***FilterBadData*** function (also in section §7.2) and defining 3 independent parameters. These three consist in a minimum accepted correlation factor (section 2.2.3), a minimum desired burst sample length and relaxation acceleration variable.

The minimum correlation factor must be set after evaluating some filtered signal profiles from the test in question. It is a way to qualify the proximity between the filtered signal shape and the expected Gaussian envelope function. For the field tests it was found that a minimum correlation of 0.25 would eliminate overlapped signals (section 3.2.2) and "blank" signals that were still, although rarely, generated even after setting a trigger requisite in both in-phase and quadrature inputs (section 2.1.2).

A minimum desired burst sample length can be a way to control the desired uncertainty in the final results, since it was found a relationship between the absolute acceleration uncertainty and the respective filtered signal length.

As mentioned in section 2.2.6 the function used to select the burst length before filtering was not always equally efficient in selecting the burst Gaussian boundaries.

This makes some of the burst signals, still with an apparent good Gaussian shape, to be suppressed due to a low correlation factor with a Gaussian envelope. In the performed tests it was found that the ones with good profile and a low correlation factor were associated with low accelerations ($<10\,\mathrm{m/s^2}$). If preferred an acceleration relaxation variable can be set to prevent such data to be eliminated.

In both the tests described, the defective signals were associated with ~ 4 to $8\,\%$ of the total data.

Figure 52 shows the histograms of the filtered velocity and acceleration data.

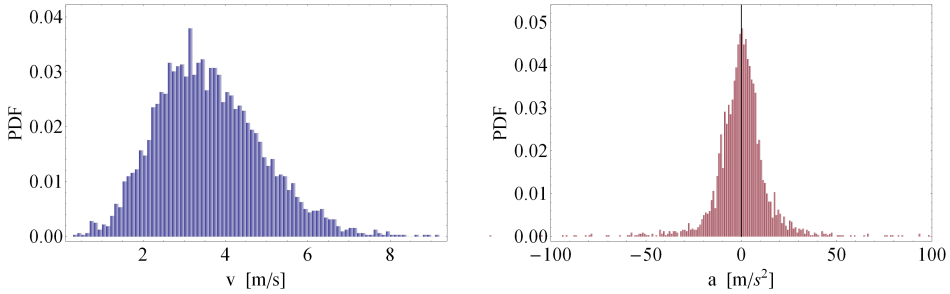

Figure 52: Filtered velocity and acceleration data histograms ($23^{rd}$of May).

If normalized by their standard deviation and represented in a logarithmic scale it is possible to see how the velocity distributions fit with a Gaussian PDF while the same does not occur with the acceleration data as mentioned in section 1.2.5. The normalized histograms with the mentioned Gaussian PDFs are represented in figure 53.

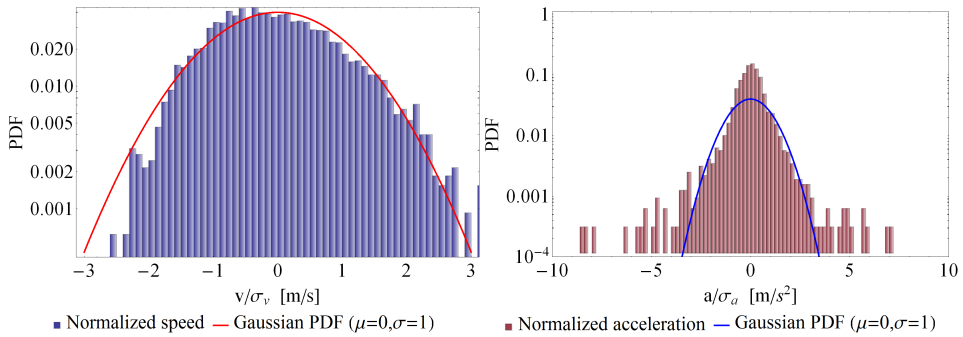

Figure 53: Filtered normalized velocity and acceleration data histograms in a logarithmic scale ($23^{rd}$of May).

The measurement of the acceleration variance, as was the experiments goal, have shown to be extremely sensitive to the ***FilterBadData*** function parameters. In fact if the bad burst samples are not rejected the acceleration variance will assume a value of $46\,960\,\mathrm{m/s^2}$. On the other hand, if filtered with a minimum correlation factor of 0.25 and a minimum signal length of 34000 samples ($\sim 0.28\,\mathrm{ms}$) with a relaxation acceleration of $10\,\mathrm{m/s^2}$ as mentioned, the data variance is then equal to $282\,\mathrm{m/s^2}$. The minimum admissible signal length was set to 34000 samples to try to restrain the measurements uncertainty to a maximum of $10\,\mathrm{m/s^2}$, according to the predictions made for the absolute acceleration uncertainty (please consult figure 39 if necessary).

Nevertheless, the acceleration variance was still found to decrease when the filtering restrictions were increased as well as the signal quality standards. This will be explored further in the present document.

In order to evaluate more accurately the acceleration variance a PDF function based on the expression in (1.24) was fitted to the data. The acceleration data was also corrected by subtracting its mean in an attempt to decrease some light pressure effects as measured in section 3.2.1. The figure 54 shows the effect of such correction in the correlation between the data histogram and the proposed PDF fitting function.

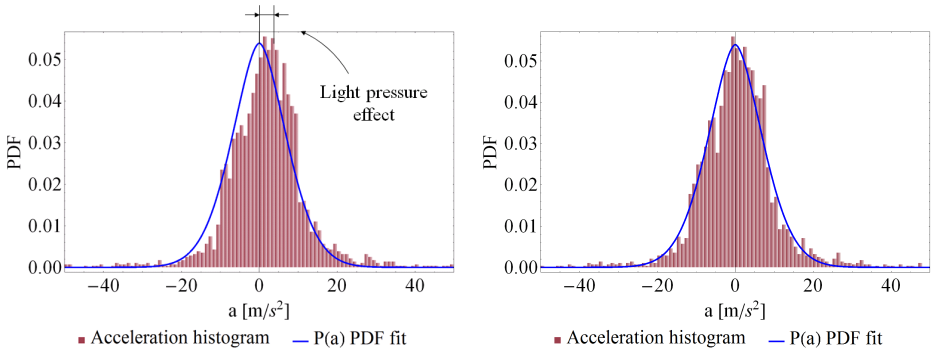

Figure 54: P(a) PDF fitting function and acceleration histograms. Filter data on the left and corrected data on the right ($23^{rd}$of May).

The acceleration variance was then determined by numerical integration over the fitting function according to (1.25), and the Kolmogorov's universal constant a_0 according to (3.9).

Since the acceleration variance parameter is extremely sensitive to the filtering function and the quality of the signals, in order to publish a final result, another evaluation was made. Due to the uncertainties in the measurements related to the burst sample length, the evolution of the variance was studied as a function of the ***FilterBadData*** permittivity for a minimum correlation factor of 0.25. The results are present in figure 55 where it is possible to see that, in this case, for a burst sample length higher than 50000 the acceleration variance starts to stabilize. By increasing the data filter parameters, as the minimum burst sample length, it is expected that the data would have less uncertainties and produce better final results. On the other hand the number of measurements considered to determine the acceleration variance decreases. Due to these reasons the results presented in table 1 are inherent to a minimum burst sample length of 50000 or (~ 0.4 ms that correspond to a predicted acceleration uncertainty $< 5\,\mathrm{m/s^2}$.

The figure 56 shows a representation of the acceleration PDF fit and measurements (using larger bins for larger acceleration values) multiplied by a^2 and a^4 respectively. These images can be compared to figure 4, from Voth [30], with which present a noted resemblance. Nevertheless both functions did not drop to zero, for the extreme acceleration measurements, as expected. This can be a way to validate the determined data distribution.

The same approach as described was applied to the data from May 5^{th} 2014 and the final results are also presented in table 1.

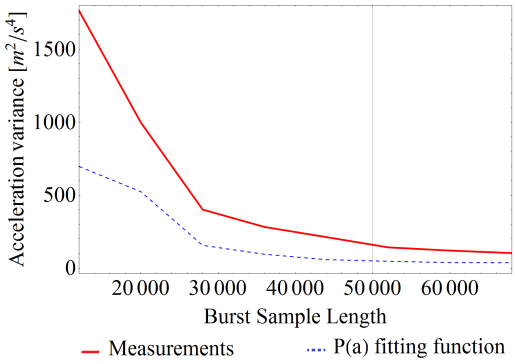

Figure 55: Effect of the ***FilterBadData*** function in the results ($23^{rd}$of May).

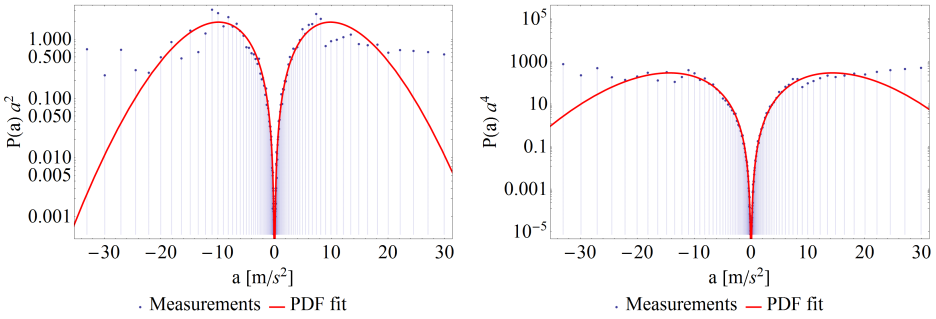

Figure 56: Acceleration PDF multiplied by a^2 and a^4 to show which events are contributing to the acceleration variance and flatness ($23^{rd}$of May).

Experiment date	$\mathbf{u_0}$ [m/s]	$\boldsymbol{\lambda}$ [m]	Re_λ	$\boldsymbol{\varepsilon}$ [m^2/s^3]	$\langle a^2 \rangle$ [m/s^2]	a0 [m/s^2]	T [ºC]	$\boldsymbol{\nu}$ $\times 10^{-6}$ [m^2/s]
23-05-2014	3.92	0.0325	2040	0.21	174	7.1	23.1	15.39
05-05-2014	2.33	0.0777	3741	0.025	64.7	64.3	12.9	14.47

Table 1: Field experiments determined parameters.

Although the experiment was inconclusive it was considered that the a_0 measurement on May 23^{rd} is probably closer to its real value, when compared to the result on May 5^{th}. This is not only supported by the fact that the obtained constant is closer to the ones from Voth measurements [30] (~ 6 for lower Reynolds numbers), but also by the fact that the function $P(a) \times a^2$ appeared to drop to zero, for large acceleration values, faster than the one obtained for the experiment on May 5^{th}.

Chapter 4

4 Conclusions

The lidar technology allows, in special conditions, the production of a signal from a single particle in which is contained information about the target speed and acceleration.

For single-particle and long signals ($\sim 1\,\text{ms}$) it is possible to guarantee low uncertainties in the measurements and infer about the wind acceleration. Nevertheless these conditions were found hard to control in a field measurement environment preventing the determination of an accurate and realistic acceleration probability density function.

Short focus distances were found to interfere with the targets motion imposing them an external acceleration due to light pressure. Nevertheless they produce high signal to noise ratio measurements and reduce the number of overlapped signals in a test when compared to long focus distances. Despite this fact, the use of long focus distances increases the probe volume, and thus, the signal time length providing e better accuracy to the measurements..

The uncertainty in the acceleration measurements was found to be inversely proportional to the signal time length (to its second power), and therefore a limitation to the proposed measurement technique since it has a fixed 120 MHz) sampling rate.

The data acquisitions system was not able to record the data at a predefined sampling acquisitions rate, adding some randomness to the determined histograms and preventing a precise determination of the desired acceleration statistical parameters.

5 Recommendations for future work

In order to evaluate the lidar possibility to return accurate acceleration measurements, the observed uncertainties must be reduced. This could be done, for example, by changing the probe volume geometry. By using a wider lens in the lidar telescope, and reducing the laser focus, a wider probe volume could also be achieved. The Gaussian beam would be less slender increasing the distance traveled by measured particle. This would increase the sample duration, decreasing its uncertainty. At the same time the probe volume should be short enough in order to guarantee a single-particle detection.

The signal filtering could be avoided if the low-pass filter would be adjusted to a new value. In fact, since the lidar is used to measure wind speeds until $\sim 40\,\text{m/s}$ say, we could filter any other frequency associated with speeds bigger than that upper bound. This would eliminate noise, associated with high frequencies, without erasing useful information and decreasing the signal processing time.

Other possible problems and limitations would be identified after these modifications applied.

[**blank page**]

6 References

[1] M. L. Chanin, A. Garnier, A. Hauchecorne, and J. Porteneuve. A Doppler Lidar For Measuring Winds in the Middle Atmosphere. *Geophysical Research Letters*, 16(11):1273–1276, 1989.

[2] Hugh W. Coleman and W. Glenn Steele. *Experimentation, Validation, and Uncertainty Analysis for Engineers.* John Wiley & Sons, Inc., third edition, 2009.

[3] DANTEC Dynamics. Laser Doppler Anemometry [LDA], 2003.

[4] F. Durst, A. Melling, and James H. Whitelaw. *Principles and Practice of Laser-Doppler Anemometry.* Academic Press, second edition, 1981.

[5] Robert Ecke. The Turbulence Problem. *Los Alamos Science*, 29:124–141, 2005.

[6] Michael Feldman. Non-linear system vibration analysis using Hilbert transform–I. Free vibration analysis method. *Mechanical Systems and Signal Processing*, 8(2):119–127, 1994.

[7] J. L. Lumle H: Tennekes. *A first course in turbuence.* The MIT Press, London, 1972.

[8] Michael Harris, Guy N. Pearson, Kevin D. Ridley, Christer J. Karlsson, Fredrik A. Olsson, and Dietmar Letalick. Single-Particle Laser Doppler Anemometry at 1.55 μm. *Applied Optics*, 40(6):969–73, February 2001.

[9] Nils Erland LeinebøHaugen. *Energy spectra and scaling relations in numerical turbulence with laboratory and astrophysical applications.* PhD thesis, Norwegian University of Science and Technology, 2004.

[10] T. W. Horst and S. P. Oncley. Corrections to Inertial-Range Power Spectra Measured by CSAT3 and Solent Sonic Anemometers,1. Path-Averaging Errors. *Boundary-Layer Meteorology*, 119(2):375–395, May 2006.

[11] Christer J. Karlsson, Fredrik A. Olsson, Dietmar Letalick, and Michael Harris. All-Fiber Multifunction Continuous-Wave Coherent Laser Radar at 1.55 μm for Range, Speed, Vibration, and Wind Measurements. *Applied Optics*, 39(21):3716–3726, July 2000.

[12] A. La Porta, Greg A. Voth, Alice M. Crawford, Jim Alexander, and Eberhard Bodenschatz. Fluid particle accelerations in fully developed turbulence. *Nature*, 409(6823):1017–9, March 2001.

[13] Jim P. Y. Lee. I/Q Demodulation of Radar Signals with Calibration and Filtering. Technical Report 1119, Establishment Ottawa, 1991.

[14] Marcel Lesieur. *Turbulence in Fluids.* Kluwer Academic Publishers, Dordrecht, third edition, 1997.

[15] Fang Lin Luo, Hong Ye, and Muhammad Rashid. *Digital Power Electronics and Alications.* Elsevier, 2005.

[16] S. Lawrence Marple. Comuting the Discrete-Time "Analytic" Signal Via FFT. *IEEE Transactions on Signal Processing*, 47(9):2600–2603, 1999.

[17] Kirk T. McDonald. Radiation Pressure of a Monochromatic Plane Wave on a Flat Mirror. Technical Report 1, Joseph Henry Laboratories, Princeton University, 2009.

[18] Bruce R Munson, Donald F Young, Theodore H Okiishi, and Wade W Huebsch. *Fundamentals of Fluid Mechanics*. Don Fowley, sixth edition, 2009.

[19] A. M. Obukhoff and A. M. Yaglom. The microstructure of turbulent flow. *National Advisory Committee for Aeronautics*, 1350, 1953.

[20] Optical Society of America. *Fiber Optics Hanbook*. McGraw-Hill, Orlando, 2002.

[21] Jagdish K. Patel and Campbell B. Read. *Handbook of the Normal Distribution*, volume 25. Marcel Dekker Inc., New York, first edition, February 1983.

[22] Alfredo Peña, Charlotte B Hasager, and Julia Lange. *E-Report: Remote Sensing for Wind Energy DTU*, volume 0029. 2013.

[23] Anders Pedersen. Conversation with Postdoc Anders Pedersen, 2014.

[24] Eagleyard Photonics GmbH. Relative Intensity Noise of Distributed Feedback Laser. Technical report, Eagleyard, Berlin, 2013.

[25] Stephen B. Pope. *Turbulent Flows*. Cambridge University Press, 2000.

[26] Bahaa E A Saleh and Malvin Carl Teich. *Fundamentals of Photonics*. John Wiley & Sons, New York, 1991.

[27] Anthony E. Siegman. *Lasers*. University Science Books, Standford, 1986.

[28] C. M. Sonnenschein and F. A. Horrigan. Signal-to-Noise Relationships for Coaxial Systems that Heterodyne Backscatter from the Atmosphere. *Applied Optics*, 10(7):1600–4, July 1971.

[29] G. I. Taylor. Statistical Theory of Turbulence. *Proceedings of the Royal Society A: Mathematical, Physical and Engineering Sciences*, 151(873):421–444, September 1935.

[30] Greg Anthony Voth. *Lagrangian Acceleration Measurements in Turbulence at Large Reynolds Numbers*. PhD thesis, Cornell University, 2000.

[31] John C. Wyngaard. *Turbulence in the atmosphere*. Cambridge University Press, NewYork, 2010.

[32] R. K. Rao Yarlagadda. *Analog and Digital Signals and Systems*. Springer, Oklahoma, 2010.

[33] Zhengji Zhang. *LDA Application Methods*, volume 36. Springer, New York, January 2011.

7 Annexes

7.1 5^{th} of May field measurements plots and results

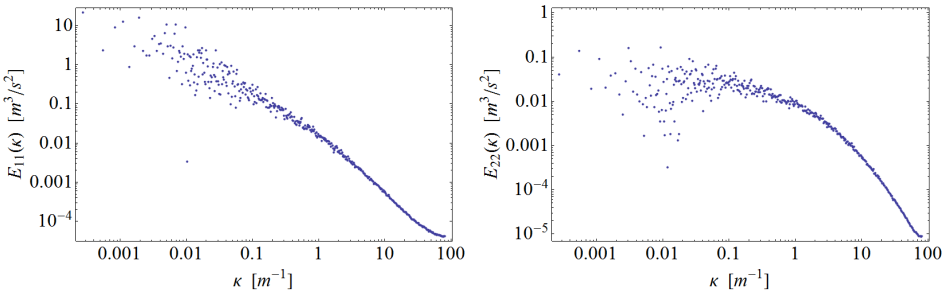

Figure 57: Energy spectra in the longitudinal and transverse direction ($5^{th}$of May).

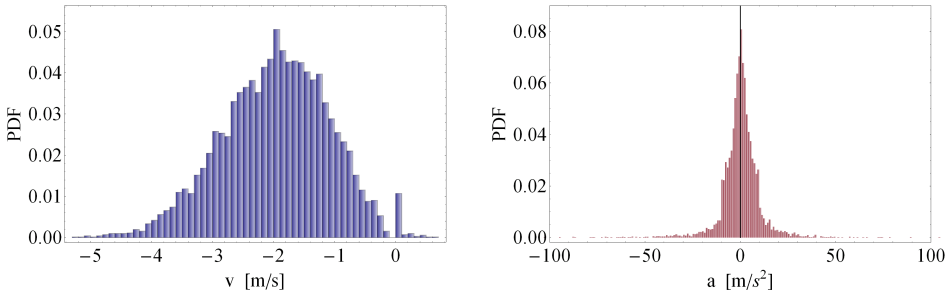

Figure 58: Filtered velocity and acceleration data histograms ($5^{th}$of May).

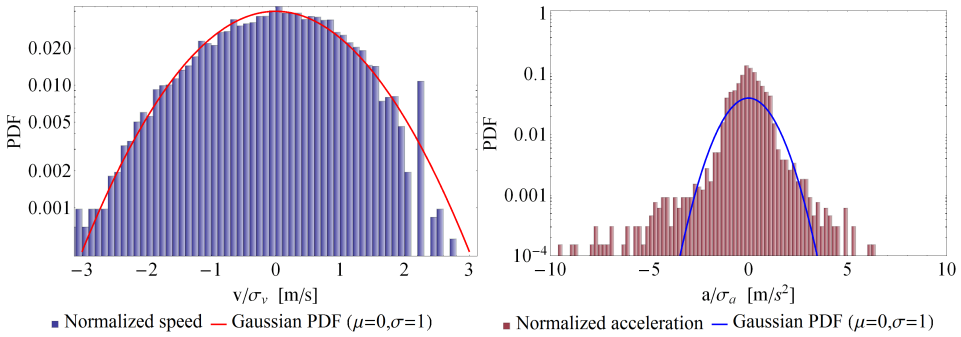

Figure 59: Filtered normalized velocity and acceleration data histograms in a logarithmic scale ($5^{th}$of May).

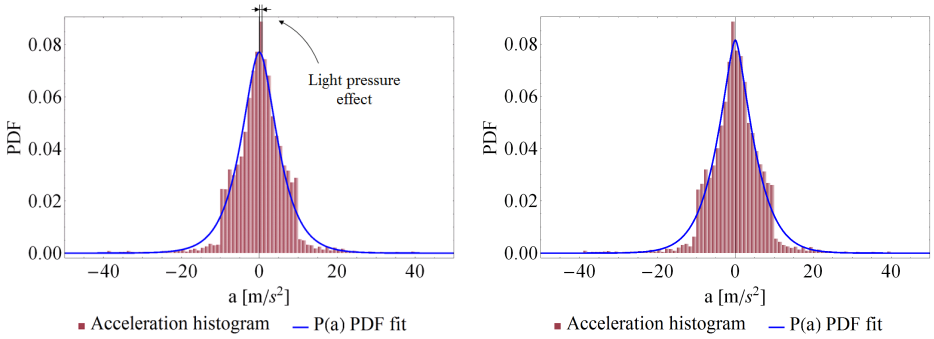

Figure 60: P(a) PDF fitting function and acceleration histograms. Filter data on the left and corrected data on the right ($5^{th}$of May).

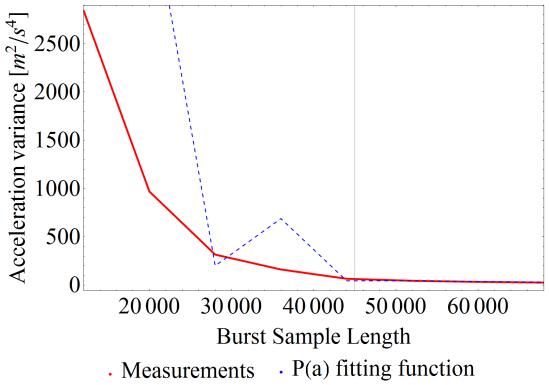

Figure 61: Effect of the ***FilterBadData*** function in the results ($5^{th}$of May).

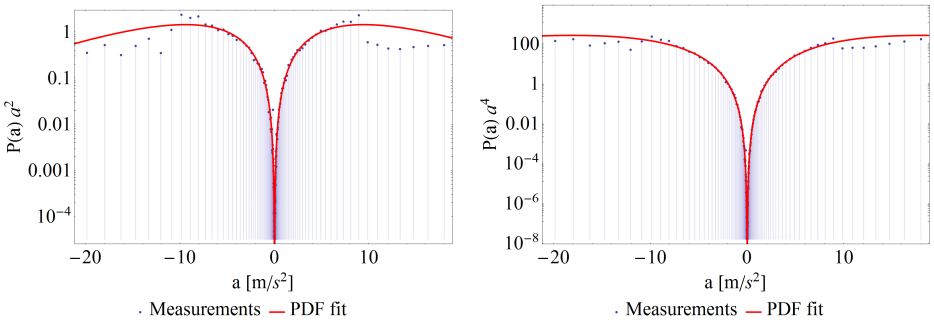

Figure 62: Acceleration PDF multiplied by a^2 and a^4 to show which events are contributing to the acceleration variance and flatness ($5^{th}$of May).

7.2 EML *Mathematica* functions and codes

The following codes, when implemented in *Mathematica*, allow the user to determine the flow speed and acceleration from the raw binary data provided by the lidar. Where is writen "DATA DIRECTORY" the user must insert his computer directory where the binary data is located. These files must be sorted by name in order to the algorithm detect the in-phase and quadrature signlas properly.

7.2.1 General properties

```
<< specan.m
   sampfreq=120 × 10^6;
   Δt = 1/sampfreq;
   fac = 1565×10^-9/(4πΔt);
```

7.2.2 Main functions

```
exp[x_] := If[x > -35, Exp[x], 0]

   Filter[ts_, n_, width_] := Module[{filt = Map[exp, -(Range[Length[ts]/2
   + 1] - n)^2/(2.  width^2)]},
   filt = Join[filt, Reverse[Drop[Drop[filt, 1], -1]]];
   Chop[InverseFourier[Fourier[ts]*filt]]]

   LocateBurst[l_] := Module[{blocksize = 10*120, var, quantile, cen,
   FWHM}, var = Variance /@ Partition[l, blocksize];
   quantile = Quantile[var, 0.75];
   var = Map[If[# < quantile, 0, # - quantile] &, var];
   (* The center is estimated by the median *)
   cen = fmed[Transpose[{Range[Length[var]], var}]];
   FWHM = Count[Map[# > 1/2 Max[var] &, var], True];
   {cen, FWHM/(2.  Sqrt[2 Log[2]])}*blocksize + {blocksize/2, 0}]

   fmed[ss_] := Module[
   {cumspec, acc = Accumulate[ss[[All, 2]]], half, p},
   If[Length[ss] == 1, Return[ss[[1, 1]]]];
   half = 0.5 acc[[-1]];
   cumspec = Transpose[{ss[[All, 1]],
   0.5 (acc + Prepend[Drop[acc, -1],0])}];
   p = Flatten[ Position[(#[[2]] > half) & /@ cumspec,
   True, 1, 1]][[ 1]];
   cumspec[[p - 1, 1]] + (cumspec[[p, 1]] - cumspec[[p - 1, 1]]) *
   (half - cumspec[[p - 1, 2]])/(cumspec[[p, 2]] - cumspec[[p - 1, 2]])]


   TakeBurst[l_, lb_, nsigma_:  3] := Module[{res},
   res = Take[l,If[Round[lb[[1]] - nsigma lb[[2]]] > 0,
   If[Round[lb[[1]] + nsigma lb[[2]]] > Length[l], Round[{lb[[1]] - nsigma
   lb[[2]], Length[l]}], Round[lb[[1]] + nsigma lb[[2]] {-1, 1}]],
   Round[lb[[1]] + nsigma lb[[2]] {0, 1}]] ];
   Transpose@If[EvenQ[Length[res]], res, Drop[res, 1]]]
```

```
FilterBurst[iqburst_, width_] := Module[{sp},
sp = Spectrum[iqburst[[1]], Length[iqburst[[1]]], 120*10^6];
cen = First@First@Position[sp[[All, 2]], Max[sp[[All, 2]]]];
Filter[#, cen, width] & /@ iqburst]

CalcPhase[iqburst_] := Module[{tmp, pha},
tmp = Arg[iqburst[[1]] + I iqburst[[2]]];
pha = Accumulate[-2πRound[Differences[tmp]/(2π)]];
pha + Drop[tmp, 1]]

hilbert[data_?VectorQ] := Module[{fopts = FourierParameters ->
{1, -1},e, n}, e = Boole[EvenQ[n = Length[data]]];
Im[InverseFourier[ Fourier[data, fopts]* PadRight[
ArrayPad[ConstantArray[2, Quotient[n, 2] - e],
{1, e}, 1], n], fopts]]] /;
And @@ Thread[Im[data] == 0]

CalcPhaseHilbert[iqburst_] := Module[{tmp, pha, temp1, arg, sign},
temp1 = Accumulate[-2π Round[ Differences[Arg[iqburst[[1]] +
I iqburst[[2]]]]/(2 π)]];
sign = Sign[temp1[[Round[Length[temp1]/2]]]];
arg = Arg[# + I hilbert[#]] & /@ iqburst;
tmp = sign*arg; pha = Map[Accumulate[-2πRound[Differences[#]/
(2π)]] &, tmp];
Table[pha[[i]] + Drop[tmp[[i]], 1], {i, 2}]]

TrimDphase[dphase_, percent_:  10] := Drop[Drop[dphase,
Round[percent/100*Length[dphase]]],
Round[-percent/100*Length[dphase]]];


Width[iqburst_] := Module[{abs, halfmax, s0, j, sigma},
abs = Abs[Fourier[iqburst]]^2;
halfmax = Max[abs]/100;
s0 = Position[abs, Max[abs]][[1, 1]];
Do[ If[abs[[i]] >= halfmax, j = i, Break[]], {i, s0, Length[abs]} ];
sigma = (j - s0)*2;
If[sigma == 0, sigma = 5, sigma = sigma]]
```

7.2.3 Initialization Code

```
SetDirectory[ "DATA DIIRECTORY"];
   FileNames[] // List;
   fil = FileNames[];
   fil = Partition[fil, 2];
   exitvector = Array[0, {Length[fil], 3}];
```

7.2.4 Code to export Bursts images along different steps

```
Do[
   SetDirectory[ "DATA DIIRECTORY"];
   fil = FileNames[]; fil = Partition[fil, 2];
   ll = Table[ BinaryReadList[fil[[j, i]], "Integer16",
   ByteOrdering -> 1]/ 2.^15, {i, 2}];
   lb = LocateBurst[ll[[1]]];
   g1 = ListPlot[ll[[1]], PlotRange -> All,
   Epilog -> Line[{{{lb[[1]] -3*lb[[2]], -1}, {lb[[1]] - 3*lb[[2]],
   1}}, {{lb[[1]] + 3*lb[[2]], -1},
   {lb[[1]] + 3*lb[[2]], 1}}}]];
   ll = Transpose[ll];
   iqburst = TakeBurst[ll, lb, 3];
   g2 = ListPlot[iqburst[[1]], PlotRange -> All];
   iqburstfilt = FilterBurst[iqburst, 2 Width[iqburst[[1]]]];
   g3 = ListPlot[iqburstfilt, PlotRange -> All];
   phase = CalcPhaseHilbert[iqburstfilt];
   dphase = Differences[(phase[[1]] + phase[[2]])/2];
   dphase = TrimDphase[dphase, 10];
   g4 = ListLinePlot[ dphase = Transpose[{Δt*Range[Length[dphase]],
   fac dphase}], Epilog -> {Red, fff[x_] = Fit[dphase, {1, x},
   x];Line[{{0, fff[0]}, {0.01, fff[0.01]}}], Text[Style["v(t) = "
   <> ToString[fff[t]], Red], Scaled[{0.5, 0.9}]]}, Joined -> True,
   Frame -> True, FrameLabel -> {"Time [s]", "Speed [m/s]"}];
   {exitvector[[j, 1]], exitvector[[j, 2]], exitvector[[j, 3]]} =
   {j, fff[Δt*Length[dphase]/2], fff'[0]};
   plotfinal = Show[GraphicsGrid[{{g1, g2}, {g3, g4}}],
   ImageSize -> 700];
   SetDirectory[ "IMAGES AND VECTOR DIIRECTORY"];
   Export[ToString[j] <> ".png", plotfinal];
   , {j, 1, 10}]
```

7.2.5 Code to only define the Speed and Acceleration Vector (SAV)

```
Do[
   ll = Table[ BinaryReadList[fil[[j, i]], "Integer16",
   ByteOrdering -> 1]/ 2.^15, {i, 2}];
   lb = LocateBurst[ll[[1]]]; ll = Transpose[ll];
   iqburst = TakeBurst[ll, lb, 3];
   iqburstfilt = FilterBurst[iqburst, 2 Width[iqburst[[1]]]];
   If[Length[iqburstfilt[[1]]] > 12000,
   ({μ, σ} = LocateBurst[iqburstfilt[[1]]];
   correlation = Correlation[ Map[Exp[-(# -μ)^2/(2 σ^2)] &,
   Range[Length[iqburstfilt[[1]]]]], Abs[iqburstfilt[[1]]]]),
   correlation = 0];
   phase = CalcPhaseHilbert[iqburstfilt];
   dphase = Differences[(phase[[1]] + phase[[2]])/2];
   dphase = TrimDphase[dphase, 10];
   dphase = Transpose[{Δt*Range[Length[dphase]], fac dphase}];
```

```
   fff[x_] = Fit[dphase, {1, x}, x];
   {exitvector[[j, 1]], exitvector[[j, 2]], exitvector[[j, 3]]} =
   {j, fff[0], fff'[0]};
   , {j, 1, Length[fil]}]
```

7.2.6 Finalization code to export and save the SAV

```
SetDirectory[ "VECTOR DIIRECTORY"];
   Export["exitvector.txt", exitvector[[]]];
```

7.2.7 Codes to statistical anaalysis

```
ZeroEraser[exitvector_, va_] := (If[va == v, j = 2];
   If[va == a, j = 3];
   exitvectoreraser = {{}, {}};
   Do[ If[Abs[exitvector[[i, 2]]] > 0.0001,
   ("exitvectoreraser=Append[exitvectoreraser,exitvector[[i,j]]]]";
   exitvectoreraser = {Append[exitvectoreraser[[1]],
   exitvector[[i, 2]]],Append[exitvector2[[2]], exitvector[[i, 3]]]})],
   {i, 1, Length[exitvector]}] ;
   exitvectoreraser[[j - 1]]);


   ProbBursts2[exitvector_, mincorrelation_:  0.25, minsamplesize_:
   12000, minacceleration_:  10] := Module[{probbursts},
   probbursts = {}; Do[ If[(exitvector[[i, 5]] < minsamplesize &&
   Abs[exitvector[[i, 3]]] > minacceleration ||
   exitvector[[i, 4]] < mincorrelation &&
   Abs[exitvector[[i, 3]]] > minacceleration),
   probbursts = Append[probbursts, i]], {i, 1, Length[exitvector]}];
   probbursts]


   EnergySpectrum[ll_, SamplFreq_, u0_] :=
   (*This one returns a -5/3 slope in the inertial subrange*)
   Module[ {n, lreal, ft}, n = Floor[Length[ll], 2];
   lreal = Partition[ll, n];
   ft = (Plus @@ (Map[(Abs[Fourier[#,FourierParameters->{0,1}]]^2)
   &,lreal])*u0)/(Length[lreal]*SamplFreq*2π);
   Transpose[ {Range[0, n/2]*N[(SamplFreq*2π)/(n*u0)],
   Take[ft, n/2 + 1]} ]];

   EnergySpectrumPlot[ll_, SamplFreq_, u0_, smooth_] :=
   (*This returns k vs E(k)k, which means the slope is -2/ 3 in the inertial
subrange*)
   Module[ {n, lreal, ft}, n = Floor[Length[ll], 2];
   lreal = Partition[ll, n];
   ft = Plus @@ (Map[(Abs[ Fourier[#, FourierParameters -> {0, 1}]]^2)
   &, lreal])/( Length[lreal]*SamplFreq);
   Manipulate[Show[{ListLogLogPlot[LogSmooth[Transpose[{Range[0,n/2]*
```

```
   N[(SamplFreq*2π)/(n*u0)],Range[0, n/2]*N[SamplFreq/n]*
   Take[ft, n/2 + 1]} ], smooth], PlotRange -> All,
   BaseStyle -> FontSize -> 24, ImageSize -> 600,
   AxesLabel -> {"κ", "E[κ]κ"}],
   LogLogPlot[ 1.5*12/55 x^(-2/3)*ϵ^(2/3), {x, 0.001, 1000},
   PlotStyle -> {Red, Thick}]}], {{ϵ, 0.022}, 0.001, 0.1, 0.001}]];

   FilterBadData[exitvector_, mincorrelation_:  0.23, minsamplesize_:
12000,
   minacceleration_:  10] :=
   Module[{evcorrected}, evcorrected = {{}, {}, {}, {}, {}};
   Do[ If[(exitvector[[i, 5]] > minsamplesize &&
   exitvector[[i, 4]] > mincorrelation ||
   Abs[exitvector[[i, 3]]] < minacceleration),
   evcorrected = Map[Append[evcorrected[[#]], exitvector[[i, #]]]
   &, Range[5]]], {i, 1, Length[exitvector]}] ; evcorrected];
```

[**blank page**]